SATELLITES, DRONES, AND CARS: AN INTEGRATED APPROACH TO URBAN HEAT ISLAND OBSERVATION

by

Max Appelbaum

(Under the Direction of J. Marshall Shepherd)

ABSTRACT

The urban heat island (UHI) is a well-known phenomenon that describes elevated air and surface temperatures in cities compared to their rural surroundings. The volume of literature on the UHI in large cities is extensive, but less work has been done for medium cities. This study focuses on the UHI in the Augusta GA-SC Metropolitan Statistical Area, a medium city along the Savannah River on the border of Georgia and South Carolina. Using satellite remote sensing of the surface UHI to inform canopy layer UHI data collection plans, a field campaign was carried out in the summer of 2023 to gather canopy layer UHI observations in Augusta via low-cost sensors mounted on a rotary unmanned aerial system and vehicle-driven traverses. Pearson correlation and ordinary least squares linear regressions were performed on the summer 2023 surface UHI and canopy layer UHI data, and these results suggest relationships to land cover.

INDEX WORDS: Urban Heat Island, Remote Sensing, Satellite Observations, Drone, UAS, Low-Cost Sensors, In-situ Observations, Urban Climate

SATELLITES, DRONES, AND CARS: AN INTEGRATED APPROACH TO URBAN HEAT ISLAND OBSERVATION

by

MAX APPELBAUM

Bachelor of Science in Atmospheric Science, University of Georgia, 2022

A Thesis Submitted to the Graduate Faculty of The University of Georgia in Partial Fulfillment of the Requirements for the Degree

MASTER OF SCIENCE

ATHENS, GEORGIA

2024

SATELLITES, DRONES, AND CARS: AN INTEGRATED APPROACH TO URBAN HEAT ISLAND OBSERVATION

by

MAX APPELBAUM

Major Professor:	J. Marshall Shepherd
Committee:	Sergio Bernardes
	Andrew Grundstein

Electronic Version Approved:

Ron Walcott
Vice Provost for Graduate Education and Dean of the Graduate School
The University of Georgia
May 2024

DEDICATION

Not to be too cliché, but this is dedicated to family and friends who have loved and supported me the whole way.

ACKNOWLEDGEMENTS

This work was supported by the Laboratory Directed Research and Development (LDRD) program within the Savannah River National Laboratory (SRNL). This document was prepared in conjunction with work accomplished under Contract No. 89303321CEM000080 with the U.S. Department of Energy (DOE) Office of Environmental Management (EM). Support for this work was also directly received from the Disruptive Geospatial Technologies Lab (DiGTL)/Center for Geospatial Research (CGR) at the University of Georgia.

TABLE OF CONTENTS

Page

LIST OF TABLES

Page

LIST OF FIGURES

Page

CHAPTER 1

INTRODUCTION

The urban heat island (UHI) is a well-studied phenomenon where urban areas experience warmer temperatures than the surrounding areas and is an important indicator of environmental conditions in and around metropolitan areas (Hutcheon et al., 1967; Kopec, 1970; KC et al., 2015; Najafzadeh et al., 2021; Oke, 1982). Urban heat island effects can modify local weather patterns and induce enhanced rainfall downwind of cities, as well as enhance lightning strike frequency (Burke & Shepherd, 2023; Rose et al., 2008; Shepherd, 2005). There are four main types of UHI that can be defined: (1) Surface UHI (SUHI), (2) Canopy Layer UHI (CLUHI), (3) Boundary Layer UHI (BLUHI) (KC et al., 2015; Najafzadeh et al., 2021; Oke, 1982; Srivanit & Hokao, 2012), and (4) Hydrologic UHI (HUHI) (Zahn et al., 2021). The SUHI is the temperature of the land surface (trees, buildings, roads, etc.). The CLUHI describes the temperature of the layer of air from the surface to the top of the urban canopy (tree canopy or rooftops), the BLUHI extends from the top of the urban canopy to the top of the urban boundary layer where the atmosphere is no longer affected by surface friction and thermal processes (often capped with a temperature inversion, ~1 km above ground level) (Oke, 1987). The HUHI describes the change in stream water temperature after rain events as precipitation interacts with hot pavement and other impervious surfaces (McCartney et al., 2020; Zahn et al., 2021) (Figure 1).

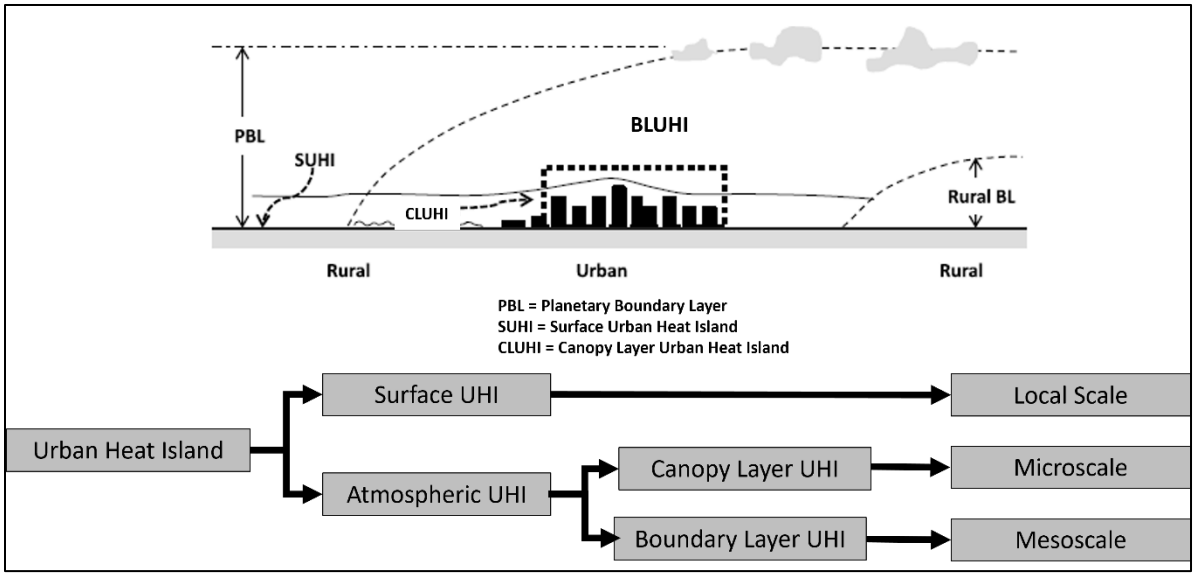

Figure 1. Hierarchy and structure of UHI types, as well as corresponding spatial scales. Hydrologic UHI spatial scale is currently undecided in the literature and therefore not included. (Modified after Kotharkar & Surawar, 2016; Oke, 1997).

Many factors within cities give rise to the UHI, but all of them are anthropogenically created. These include greenhouse gas (GHG) and pollutant emissions, waste heat from industry and building cooling, impervious and dark surfaces such as roads and buildings, the three-dimensional geometry of the urban area, and environmentally detrimental landscape modification (i.e. replacing healthy greenspace with impervious surface cover) (Zahn et al., 2021; Zhou et al., 2017).

It is estimated that by 2050, 68% of the world's population will live in urban areas, having risen from 55% in 2017 (Ritchie & Roser, 2018). It can be reasonably assumed that as urban populations swell and population densities increase, the intensities of UHI's around the world will increase if mitigation techniques are not put into place. Examples of strategies to mitigate UHI's include using reflective building materials, enhancing urban greenery, and

systems to dissipate heat to lower temperature sinks (Santamouris et al., 2018; Zhou & Shepherd, 2009). However, these strategies can be expensive and difficult to implement; therefore, targeting hot intra-SUHI's for mitigation efforts will reduce the costs of attempting to implement a blanket city-wide plan.

The urban heat island effect of large cities (typically defined as greater than 1 million residents) is well-studied, with new literature being published frequently, including many inter-city comparison studies (Hsu et al., 2021; Peng et al., 2011; Ramamurthy and Sangobanwo, 2016; Li et al., 2020). Although it was observed as early as 1970 that cities with a population as small as 25,000 people can exhibit urban heat signatures (Kopec, 1970), there is considerably less work in the literature regarding the UHI of medium and small cities, and nearly all focus on a single city without attempting inter-city comparisons (Cardoso et al., 2017; Hedquist and Barker, 2016; Stathopoulou and Cartalis, 2007).

In an effort to continue filling knowledge gaps regarding the UHI of medium cities, this thesis conducts a multi-instrument observational urban heat island study for the Augusta, Georgia-South Carolina Metropolitan Statistical Area (Augusta MSA) as defined by the US Census Bureau (Figure 2). The Augusta MSA comprises of Lincoln, McDuffie, Columbia, Richmond, and Burke counties in Georgia, and Edgefield and Aiken counties in South Carolina. The total area of the Augusta MSA is 3,408.7 square miles, is approximately 100 miles from the Atlantic coast at its nearest point and lies along the path of the Savannah River. Across all seven counties, the Augusta MSA has a combined population of 616,395 (US Census Bureau, 2021).

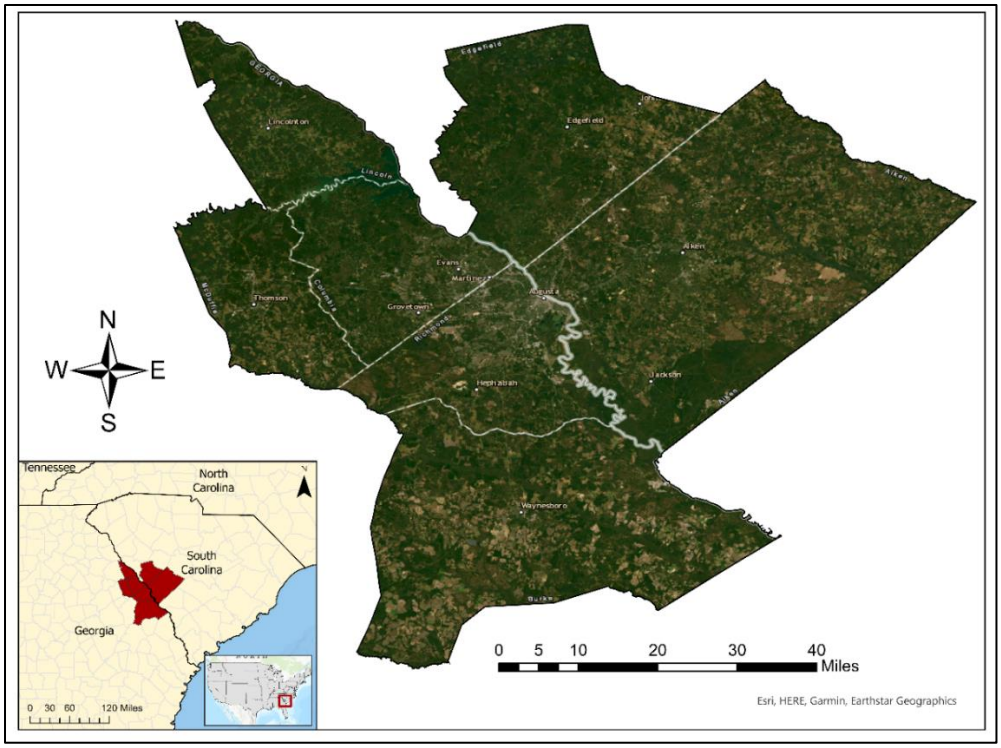

Figure 2. Augusta, GA-SC Metropolitan Statistical Area.

This study is also designed with the thought in mind that future studies stemming from this work will utilize the gathered data to more closely investigate the UHI in Augusta through the lens of neighborhood-level heat exposure and possible socioeconomic factors that may increase risks to vulnerable populations. The city of Augusta is in Richmond County, Georgia, established as a consolidated city-county government, and has a population of 202,081 people. Demographically, Augusta is majority black or African American at 56.5%, and 34.7% of the population is white. Additionally, 22.1% of the population lives at or below poverty level. These demographic facts reveal that Augusta is likely vulnerable to disproportionate heat exposures due to urban heat island effects, as a study of urban heat exposure in 175 American cities found that members of minority populations and those living in poverty are exposed to up to 2ºC more heat than non-Hispanic whites and those earning above two times the poverty line (Hsu et al., 2021)

(Figure 3). A 2019 study of 25 cities around the world found similar results, with 72% of sampled cities showing elevated heat exposure in poorer neighborhoods (Chakraborty et al.). Thus, Augusta and the greater MSA can greatly benefit from a possible first-ever in-depth analysis of the urban heat island effects that can inform planners and stakeholders of the heat exposure risks that are unique to their area and inform decisions to mitigate the urban heat as much as possible.

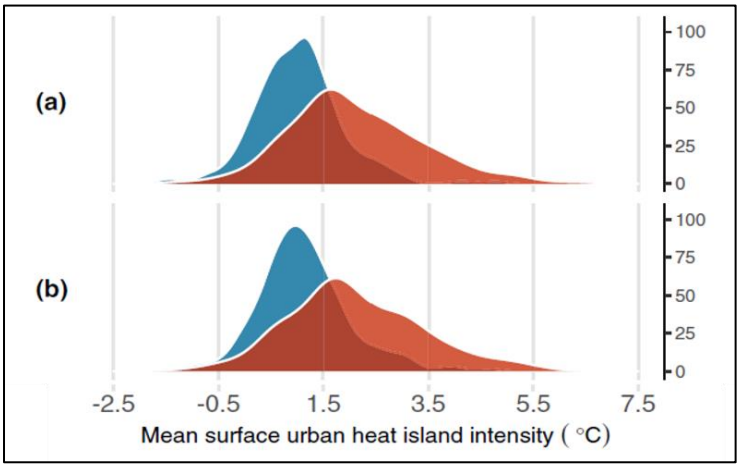

Figure 3. Adapted from Hsu et al. (2021). Showing: (a) Non-Hispanic white people (blue) vs. all people of color (red) and (b) 2x above poverty (blue) vs. below poverty (red).

Research Questions and Objectives

1. What is the intensity and influencing land cover factors of the surface UHI and intra-SUHI's of the Augusta, Georgia Metropolitan Statistical Area, and how can this be used to inform in-situ canopy layer UHI observation planning?
2. What land cover factors most influence Augusta's near-surface canopy layer UHI intensity, as observed via vehicle-borne low-cost sensor collections?
3. How can unmanned aerial systems (UAS) and low-cost sensors be best integrated to observe canopy layer UHI vertical structure?

CHAPTER 2

LITERATURE REVIEW

Surface UHI Methods

The surface (or skin) urban heat island (SUHI) is a phenomenon that describes the disproportionate warming of impervious urban surfaces compared to their more rural surroundings (Bärring et al., 1985; Chakraborty et al., 2019; Johnson & Shepherd, 2018; Peng et al., 2011; Srivanit & Hakao, 2012; Zhou et al., 2017). This arises due to the thermal characteristics of impervious urban surfaces that allow them to absorb more solar radiation than natural pervious surfaces and to hold onto this heat for longer into the evening due to their high heat capacity. This means that SUHI intensity, the difference between urban and rural land surface temperatures, will typically peak in the late evening after sunset (Qian et al., 2022; Zhou & Shepherd, 2009). Net radiative imbalances in the surface energy budget between the urban and rural surfaces (Figure 4) can have a great effect on local meteorological conditions, including the enhancement of rainfall (observed and reported in Augusta by McLeod et al., 2024) and lightning strike frequency downwind of the city (Burke & Shepherd, 2023). It should be noted that these meteorological modifications are also influenced by other urban factors such as urban canyon geometry and building height, among others (Dixon & Mote, 2003; Rose et al., 2008; Shepherd, 2005).

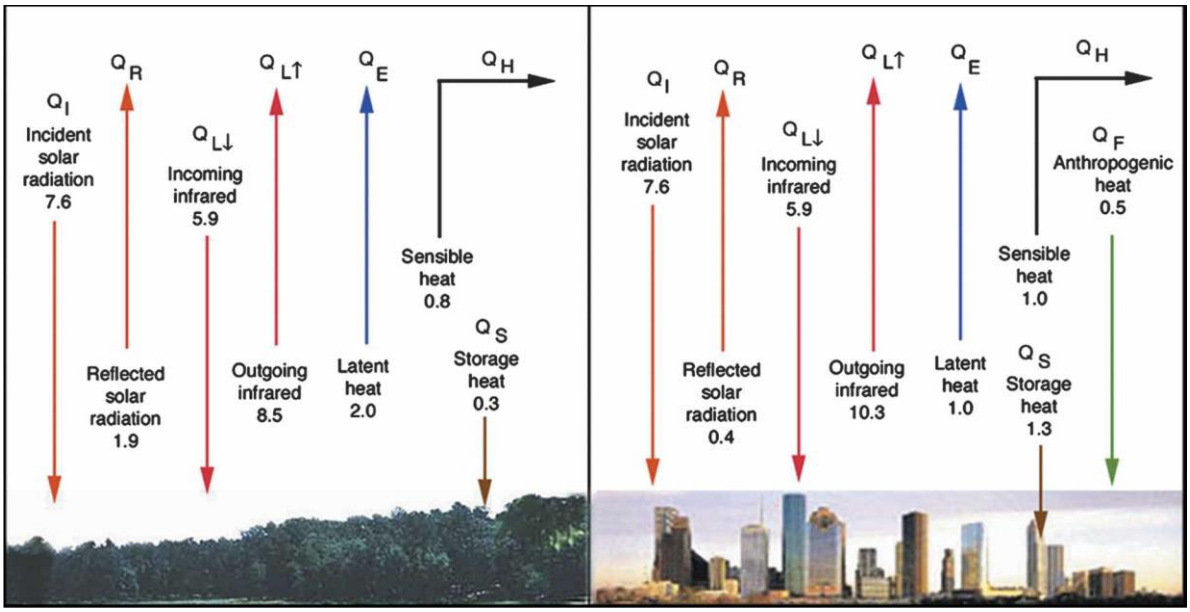

Figure 4. Radiative energy balances for rural areas (left) and urban areas (right), values are in kW h m^2 day^{-1} (courtesy of R. Sass, Rice University, online at http://www.ruf.rice.edu/~sass/UHI.html).

Within the SUHI, Han et al. (2021) identified the presence of intra-urban SUHI's (intra-SUHI's) in Shanghai, China. Intra-SUHI's are local areas of notably hot or cold surface temperatures within cities, and Han et al. defined intra-SUHI's as being in the 5th and 95th percentile thresholds on the cumulative probability curve of their normal distribution. Intra-SUHI's may be of interest to researchers and city planners because ground surveys of these areas can reveal what urban factors are either enhancing or reducing temperatures. By learning the factors that can make an area into a cold intra-SUHI, planners can identify heat mitigation strategies that will be the most effective in their specific city.

The advent of thermal infrared satellite remote sensing and advancements in geographic information science (GIS) techniques allowed for observation of the land surface temperature, and therefore surface urban heat island, accurately and over an essentially unlimited study area

(Gallo et al., 1995; Jin et al., 1997; Price, 1979; Streutker, 2002). In the majority of modern literature, two families of earth-observing satellites are used to observe the SUHI: the Moderate Resolution Imaging Spectroradiometer (MODIS) family (Del Pozo et al., 2020; Tariq et al., 2022; Wu et al., 2019) and the Landsat family (Advan & Jovanovska, 2016; Kaplan et al., 2018; Miky, 2019; Šalkovič et al., 2023; Wang et al., 2015). Both satellite families are operated by NASA with data provided freely to the public.

The first MODIS instrument was launched in 1999 and the second was launched in 2002, both providing 36 spectral bands, including thermal infrared (NASA, n.d.-a). As of 2008, MODIS has provided processed and ready-to-use LST products at 1km spatial resolution, revalidated in 2008, with data available from 2000 onward (NASA, n.d.-b). MODIS also provides a very large image swath of 2,330km with images provided in 10^{o} x 10^{o} tiles, allowing for wide spatial coverage in one image.

Landsat 4, launched in 1982, carried the first thermal infrared-capable sensor onboard a Landsat satellite and provided a thermal spatial resolution of 120m ("Landsat 4", n.d.), and all subsequent Landsat satellites carried a thermal infrared band (now 100m resolution on Landsat 8 and 9) ("Landsat 8", n.d.; "Landsat 9", n.d.). Unlike MODIS, Landsat imagery is often processed by the user to calculate LST from raw digital number data. Landsat is limited in the number of spectral bands available when compared to MODIS, with only 11 spectral bands. Landsat provides an image swath of 185km, making it useful for smaller study areas. Additionally, MODIS can provide daily temporal resolution, while Landsat 8/9 provides an eight-day temporal resolution.

Each satellite family has its own strengths and weaknesses that might make one better suited for certain tasks than the other. For example, as mentioned above, MODIS can enable

studies of large geographic areas, however, Landsat provides much higher spatial resolution than MODIS does (100m in thermal for Landsat 8/9 and 1km in thermal for MODIS). Comparing the trade-offs between the two, MODIS imagery is better suited for urban heat studies that focus on a large area and inter-city comparison studies, as the lower spatial resolution will allow for faster processing times. Landsat imagery, therefore, is better suited to smaller study areas where finer spatial resolution is desired for within-city studies.

Canopy Layer UHI Observation

Originally known as just "the heat island" or "the urban heat island" (Kopec, 1970), the canopy layer urban heat island (CLUHI) describes elevated air temperatures from just above the ground surface to the height of the canopy (building height or tree height) in urban areas when compared to their rural surroundings (Johnson & Shepherd, 2018; Oke, 1982). The CLUHI has traditionally been observed with either vehicle-borne temperature loggers (Hutcheon et al., 1967; Kotharkar & Surawar, 2016; Wong & Yu, 2005; Y. Yin et al., 2021) or by using local meteorological station data (Bärring et al., 1985; Tariq et al., 2022; Zhou & Shepherd, 2009).

In the literature there are two approaches to vehicle-borne CLUHI observations, and each has their own benefits and drawbacks. The first is to observe the conditions on a linear rural-urban-rural transect (Cardoso et al., 2017; Hutcheon et al., 1967; Kotharkar & Surawar, 2016), and the second is to plan a traverse that winds through the study city (Kopec, 1970; Wong & Yu, 2005; Y. Yin et al., 2021). The transect approach has the advantage of being able to observe temperature gradients from rural-urban-rural and can enable more direct comparisons between urban and rural conditions. However, a linear transect may over-simplify the true nature of the CLUHI by potentially missing areas that may be the hottest or coldest. A traverse collection, on the other hand may not be best suited to observing rural-urban-rural gradients but allows

observation of the intra-city spatial patterns of the CLUHI and can be more useful for studies with thoughts towards examining heat exposure differences between neighborhoods. Since future studies stemming from this project are planning to investigate Augusta in this manner, a traverse was selected as the vehicle collection method in this study.

UAS for Meteorological Observation

With the growing popularity of unmanned aerial systems (UAS) in scientific research, a growing number of studies have explored the use of rotary UAS for atmospheric soundings and observations of the lower atmosphere. As this is such a new observation tool, there is yet to be a general consensus in the literature as to the best methods and sensors to use. There are two main approaches to UAS atmospheric instrumentation: off-the-shelf products like the iMet XQ2 (Inoue & Sato, 2022; Varentsov et al., 2023), and novel Arduino- or Raspberry Pi-based systems (Chang et al., 2020; Chilson et al., 2019; Chodorek et al., 2021). By choosing to use an off-the-shelf product, the user will usually sacrifice high accuracy for moderate accuracy, but the installation and setup will be much easier than assembling a novel sensor system. However, off-the-shelf products such as the iMet XQ2 are expensive (~$500) for small-budget projects. A novel system may take more time and effort to initially set up, but the resulting accuracy and cost savings currently make this approach the best option for maximizing a limited budget.

To date, there have been very few studies that have explored the applications and potential benefits of UAS observations for UHI studies. Chodorek et al. (2021) conducted a pilot study to experiment with UAS weather sensing in an urban environment using low-cost sensors, and their results showed strong performance when compared with a calibrated weather station. However, as this study was meant primarily for sensor testing and validation, their test flights were conducted at only one location. The most comprehensive study that has been conducted

thus far using UAS for UHI investigation comes from Varentsov et al. (2023) in their study of urban boundary the urban boundary layer in the Arctic Western Siberian city of Nadym. In addition to a series of surface weather stations that were deployed in a linear transect across the city, they also utilized three UAS in three locations along the transect. One of their flight points was outside of the city, one flight point was inside, but near the edge of the city, and the third flight point was in the city center. This allowed them to observe urban boundary layer formation and decay over a diurnal cycle over several periods of observation. In their study, they concluded that utilizing UAS to observe urban heat island vertical structure is highly valuable and can enable micro-scale studies that have not previously been possible.

CHAPTER 3

SURFACE UHI METHODS

This chapter will solely discuss the data and methods used for surface urban heat island remote sensing. Resulting maps are presented in Chapter 4 of this document.

Land Surface Temperature Retrieval

The land surface temperature was retrieved using thermal satellite imagery from the Landsat Land Surface Temperature (LST) Bundle that is provided free of charge via the United States Geological Survey's "EarthExplorer" data portal (https://earthexplorer.usgs.gov/). The LST bundle contains atmospherically corrected surface temperature derived from the thermal infrared (TIR) band 10 of Landsat 8 and Landsat 9, pixel quality control bands for masking purposes, and the raw imagery used in their surface temperature calculations. To calculate LST, they apply the Single-Channel Algorithm (Jiménez-Muñoz & Sobrino, 2010), rather than the Split-Window Algorithm (Qin et al., 2001) due to data quality issues with TIR band 11 of Landsat 8. The Single-Channel Algorithm developed by Jiménez-Muñoz & Sobrino is as follows:

$$B(LST) = \frac{L_{sen} - L_{up} - \tau(1-\varepsilon)\cdot\frac{L_{down}}{\pi}}{\tau\cdot\varepsilon}$$

where B is the Planck function, L_{sen} is at-sensor radiance, L_{up} is thermal path radiance, L_{down} is downwelling irradiance, τ is atmospheric transmissivity, and ε is surface emissivity.

Specifically, Band 10 Surface Temperature (ST_B10), Band 10 QA (ST_QA), and Pixel QA (QA_PIXEL) is used from the LST Bundle in 30m x 30m resolution. The 100m x 100m resolution TIR band 10 is resampled to a finer spatial resolution by using 30m x 30m imagery

from the operational land imager (OLI) blue, green, red, and near IR bands in surface emissivity calculations. From ST_QA, pixels with a surface temperature uncertainty greater than 5 Kelvin were masked. From QA_PIXEL, pixels not matching the pixel value for fully clear conditions.

For analysis of only land surface temperature with no water contamination, stream and waterbody shapefiles were used to mask those features. These shapefiles are freely available from the National Hydrologic Dataset, and accessible from the United States Geological Survey's National Map online data portal (https://apps.nationalmap.gov/downloader/).

Surface UHI Intensity

Surface urban heat island intensity is calculated by taking the difference between the observed LST of within the urban area and the observed LST of a nearby rural area (Buyantuyev & Wu, 2010; Yuan & Bauer, 2007). For this study, the rural control was taken as the mean LST of all counties conterminous to the MSA that is covered by the Landsat scene. Such a broad area was chosen to capture the mean LST of both rural towns and natural land cover, such as forests and open fields.

For the first general visualization of the SUHI in the full Augusta MSA over all months, eighty-eight cloud-free (< 10%) images spanning 2019-2021 from the Landsat LST Bundle were used. The Augusta MSA is very large in terms of land area (3,408.7 mi^2), and its geographic location straddles the intersection of four Landsat image footprints (Figure 5). Therefore, the eighty-eight total images used for the large area analysis actually represent twenty-two days of cloud-free imagery for all months between 2019 and 2021, with four images being mosaicked to represent collections one week apart.

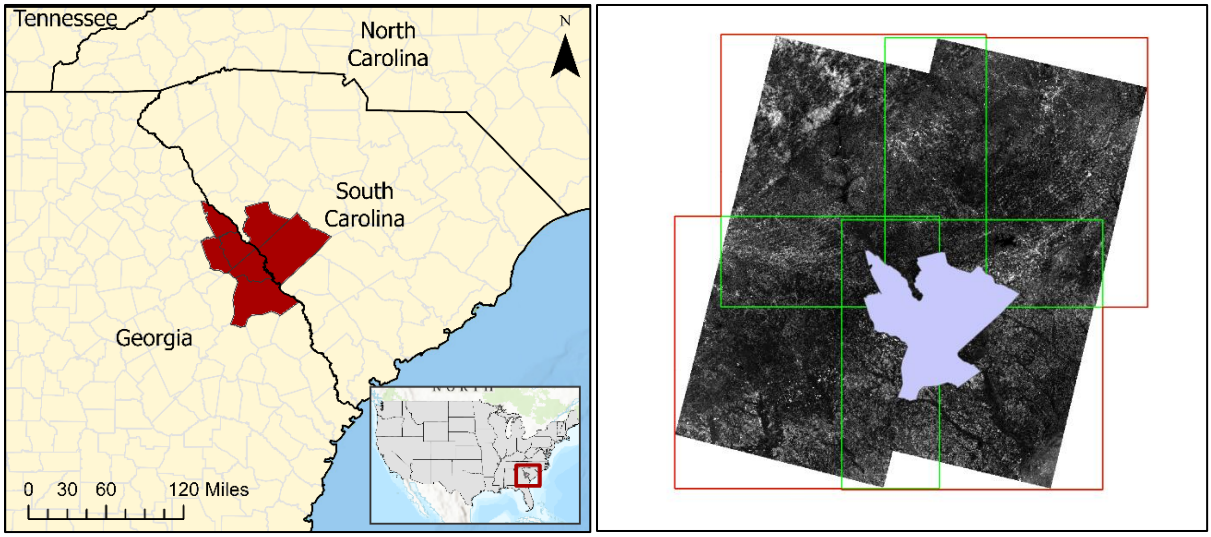

Figure 5. Augusta MSA and example image mosaic

Intra-Urban Surface UHI Identification

Intra-urban surface urban heat islands (intra-SUHI) were identified via percentile thresholds on the cumulative probability curve of LST. In Shanghai, China, Han et al. (2021), identified intra-SUHI's as belonging to the 5th (cold intra-SUHI) and 95th (hot intra-SUHI) percentile observed LST at the time of observation by Landsat 8, and they found that this technique results in tighter hotspot classification than standard deviation classification. Standard deviation techniques showed very broad areas of hot spots and did not identify cold spots as well as percentile thresholds were able to.

For these reasons, the methods of Han et al. (2021) were chosen to identify intra-SUHI's in Augusta. However, Augusta is a much smaller city than Shanghai both in terms of population and urban sprawl and may show smaller signals of SUHI intensity and higher spatial heterogeneity of SUHI intensity by having a smaller and generally less dense central urban core. Thus, then 10th and 90th percentile values were also considered to indicate cold and hot intra-SUHI's, respectively.

The use of satellite imagery that is collected at a single moment in the day limits the ability to identify daily maximums and minimums or possible changes to the spatial distribution of intra-SUHI's (Y. Yin et al., 2021). However, it is not currently feasible to observe this phenomenon without the use of high-resolution computer models or specially commissioned high-resolution aerial imagery, therefore, Landsat TIR imagery has become very popular in remote sensing studies of SUHI's and intra-SUHI's (Estoque & Murayama, 2017; Kaplan et al., 2018; Najafzadeh et al., 2021).

To create a high-detail map of the intra-SUHI's in central urban core of the Augusta city area to inform traverse delineation for CLUHI observation, the analysis domain was reduced (Figure 6). The primary reason for this change was to be able to use a single image footprint and avoid the need for a mosaic. The original plan was to use imagery from the summer of 2022 in order to have the most up-to-date visualization possible, however, only one cloud-free image was available (June 16, 2022). The summer (JJA) of 2021 had zero cloud-free images available. Therefore, the image search was extended back to JJA 2020 and yielded three additional cloud-free images (July 11, July 27, August 12, 2020) to be used in the high-detail visual analysis for traverse delineation. As the purpose of these first visualizations of the SUHI are primarily for visual analysis of the general spatial pattern and to aid in field planning, statistical analyses were not conducted on these initial results.

This same urban core study domain was on imagery from JJA 2023 to temporally coincide with in-situ observations of the CLUHI. There were six cloud-free (< 10%) images from JJA 2023: June 10, June 18, June 26, July 4, August 13, and August 29.

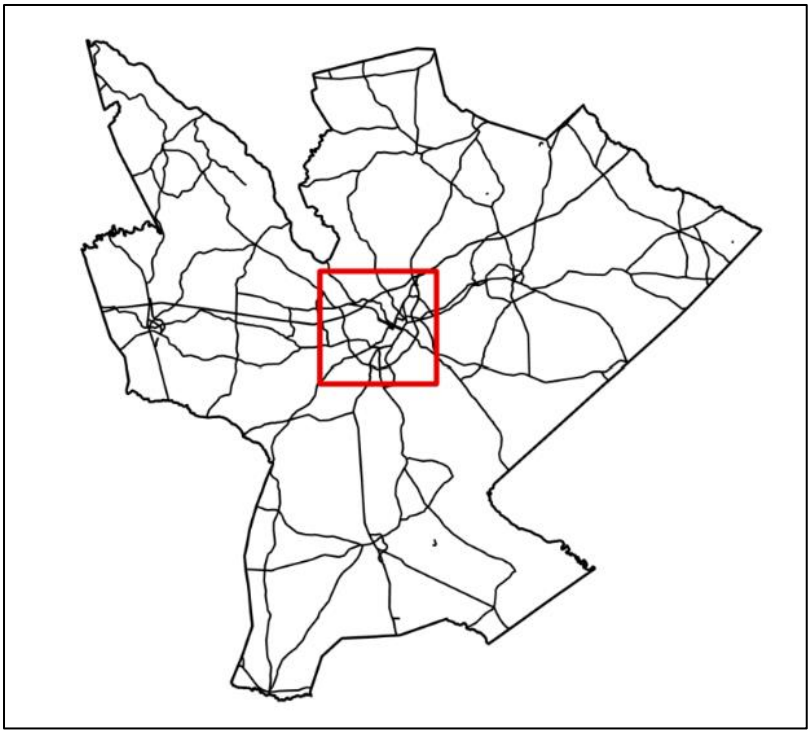

Figure 6. Augusta MSA with urban core field collection domain (red box, right)

Relationships to Land Cover

Pearson correlation coefficient (Han et al., 2021; Zhou et al., 2014) and Ordinary Least Squares (OLS) linear regression statistical analyses (Buyantuyev & Wu, 2010; Estoque & Murayama, 2017; Yuan & Bauer, 2007) were applied to the JJA 2023 urban core study domain SUHI results to quantitatively investigate the influence of various land cover types on SUHI intensity. The land cover types investigated via Pearson correlation coefficients were normalized difference vegetation index (NDVI) to serve as a proxy for overall vegetation density, as well percent impervious surface cover and percent tree cover from the National Land Cover Database 2021 (NLCD 2021). Pearson Correlations are not suited for categorical variables (Baak et al., 2020), thus NLCD 2021 class was not included for correlations. The same land covers were investigated via OLS regressions. Additionally, the categorical National Land Cover Database

2021 and a bivariate model of tree cover and impervious surface percent was also included in the regressions. NDVI was calculated using band 4 (red) and band 5 (near infrared) of Landsat 8 and Landsat 9's Enhanced Thematic Mapper + (ETM+) with Level-2 atmospherically corrected imagery from the same dates used for the JJA 2023 SUHI and intra-SUHI, downloaded from the USGS "Earth Explorer" data portal. The calculation for NDVI is as follows (Sunardi et al., 2019):

$$NDVI = \frac{(NIR - R)}{(NIR + R)}$$

where *NIR* is equal to Landsat 8 and 9 ETM+ band 5, and *R* is equal to Landsat 8 and 9 ETM+ band 4.

To minimize potential biases imparted by spatial autocorrelation, one random sample of 500 points from the urban core study area, and one from random sample of 500 points the rest of the MSA that was covered by the JJA 2023 imagery. Following recommendations of existing and well-cited literature (Buyantuyev & Wu, 2010; Yuan & Bauer, 2007; Zhou et al., 2014), a minimum distance of 300 meters between points was assigned during the random selection.

CHAPTER 4

SURFACE UHI TO INFORM IN-SITU DATA COLLECTION PLANNING

This chapter presents the results of the first SUHI visualization and intra-SUHI characterization with imagery from all months 2019-2021 and JJA 2020 and 2022, respectively, how this informed CLUHI data collection planning, and the resultant data collection field plan.

Augusta MSA Surface UHI: All Months 2019 - 2021

The analysis of Landsat thermal imagery from all months 2019-2021 revealed that the medium city of Augusta does display a SUHI signature, up to 15°C above the rural mean LST (16.1°C) (Figure 7).

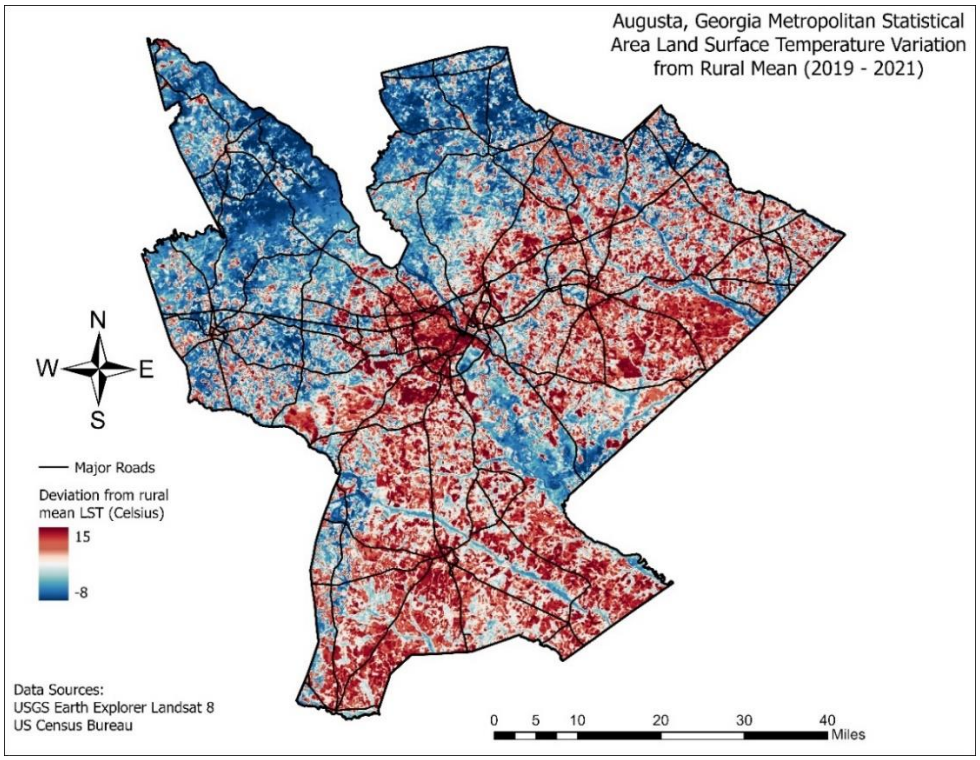

Figure 7. Surface urban heat island for the Augusta MSA, 2019 – 2021. Light blue is *zero urban-rural delta.* Data Source: Landsat LST Bundle.

Visual analysis of Figure 7 shows a clear urban heat signature in the central urban core of the Augusta MSA (indicated in Figure 6) and surrounding suburban areas where urban landcover and impervious surfaces are predominant (Figures 8, 9). The ~~northeastern~~ northwestern area of the MSA shows the coolest surface temperatures where forested land cover dominates (Figure 10). The southern and eastern portions of the MSA show moderately elevated LST, likely due to large crop fields that heat up quickly during the day.

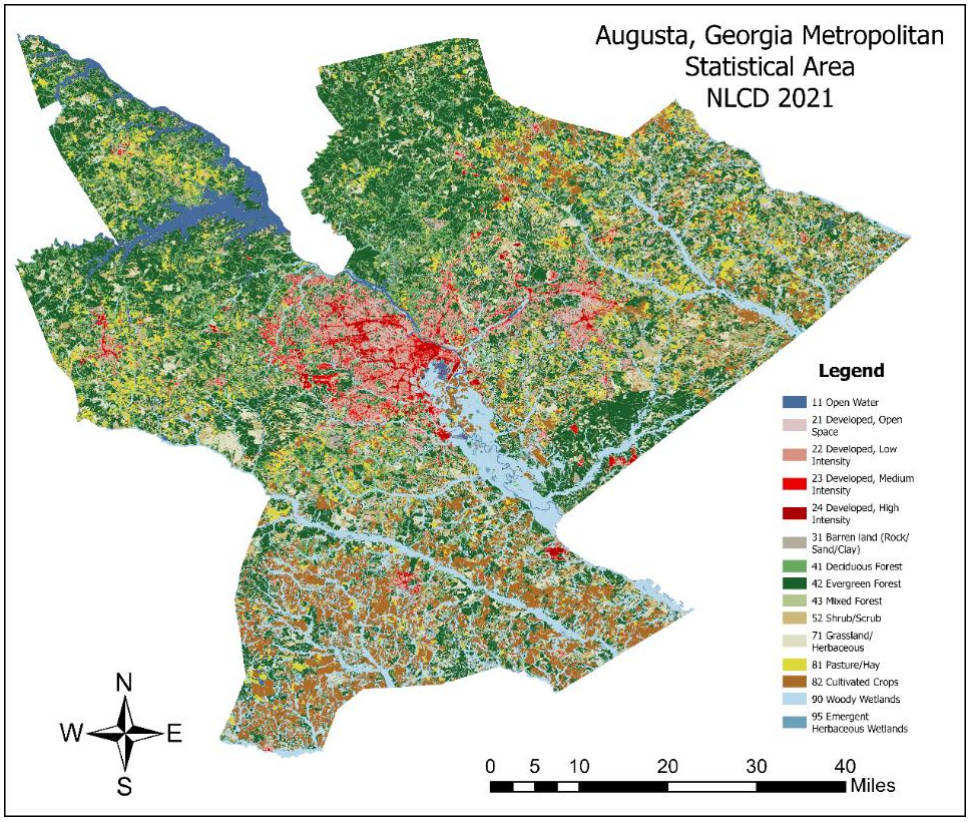

Figure 8. Land Cover Type. Data Source: 2021 National Land Cover Database.

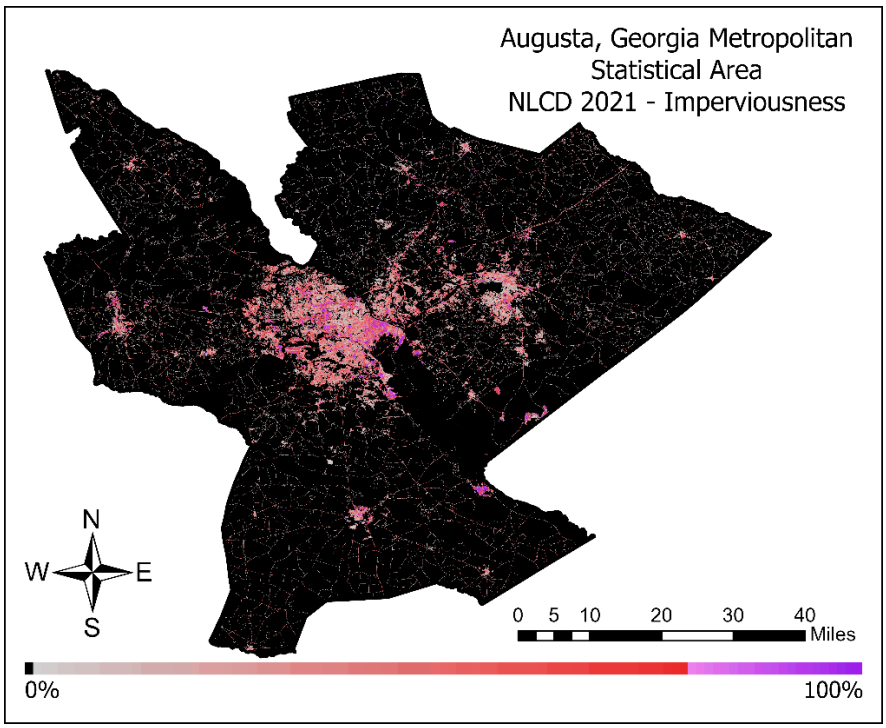

Figure 9. Impervious surface coverage. Data Source: 2021 National Land Cover Database.

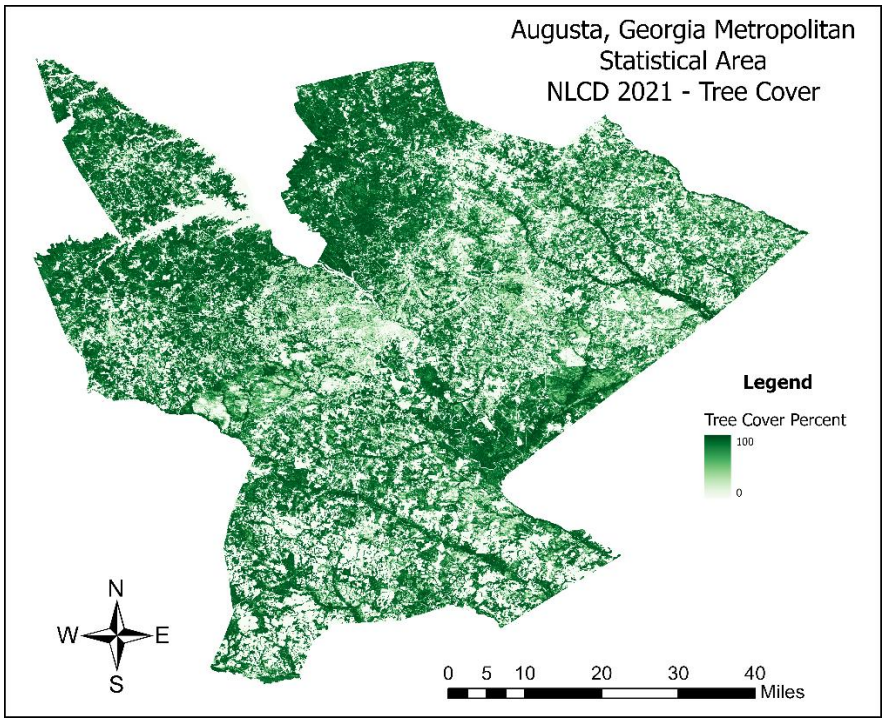

Figure 10. Tree cover. Data Source: 2021 National Land Cover Database.

Augusta Urban Core Intra-SUHI: JJA 2020, 2022

The urban core of the Augusta MSA shows a complex anatomy of hot and cold intra-SUHI's with a peak intensity of 24.8°C above the rural mean. Hot spots appear to correspond (90th percentile = +3.4°C, 95th percentile = +4.1°C) with areas with higher impervious surface coverage and denser buildings, while cold spots (10th percentile = -1.9°C, 5th percentile = -2.2°C) appear to correspond to areas with more vegetation or that are nearby to water (Figure 11). By revealing localized areas of much warmer or much cooler SUHII, intra-SUHI maps such as this can be used to inform in-situ canopy layer UHI observations by indicating possible areas of interest for further investigation (Figure 12).

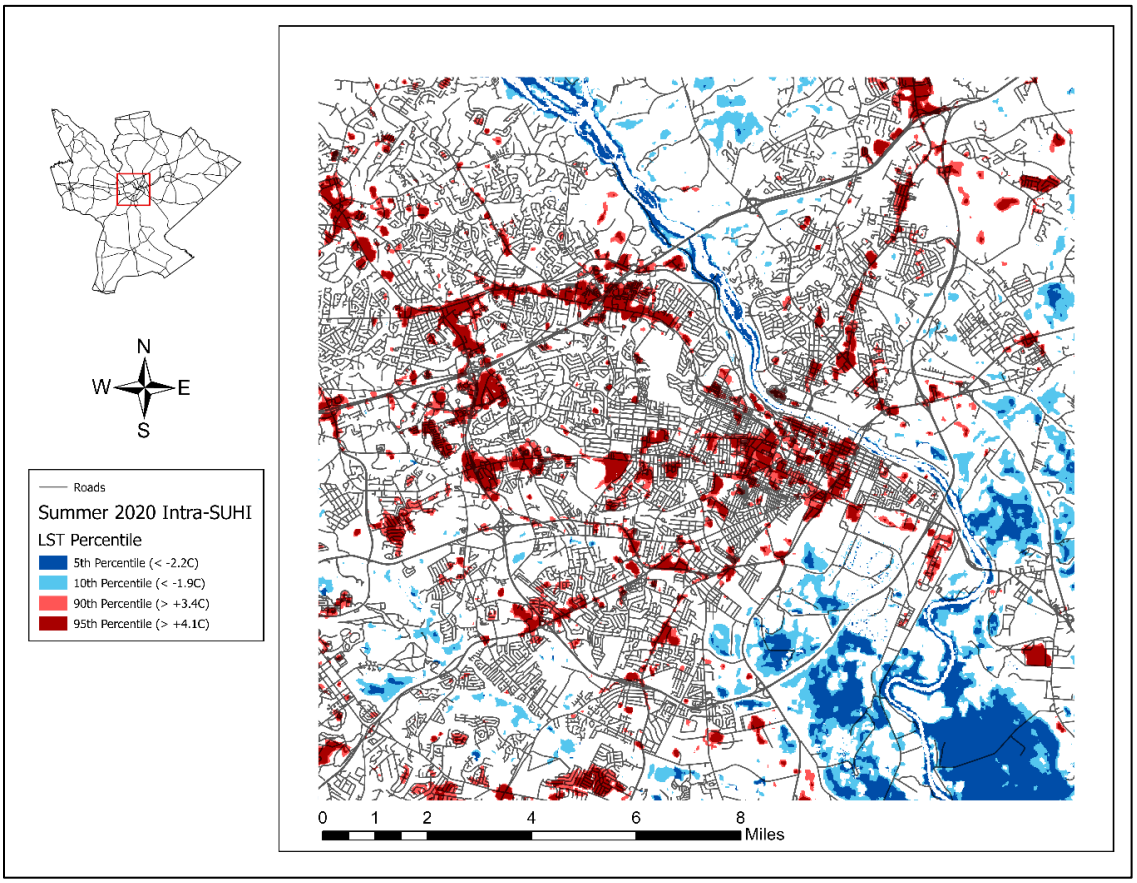

Figure 11. Intra-SUHI for JJA 2020 and 2022. Data Source: Landsat LST Bundle.

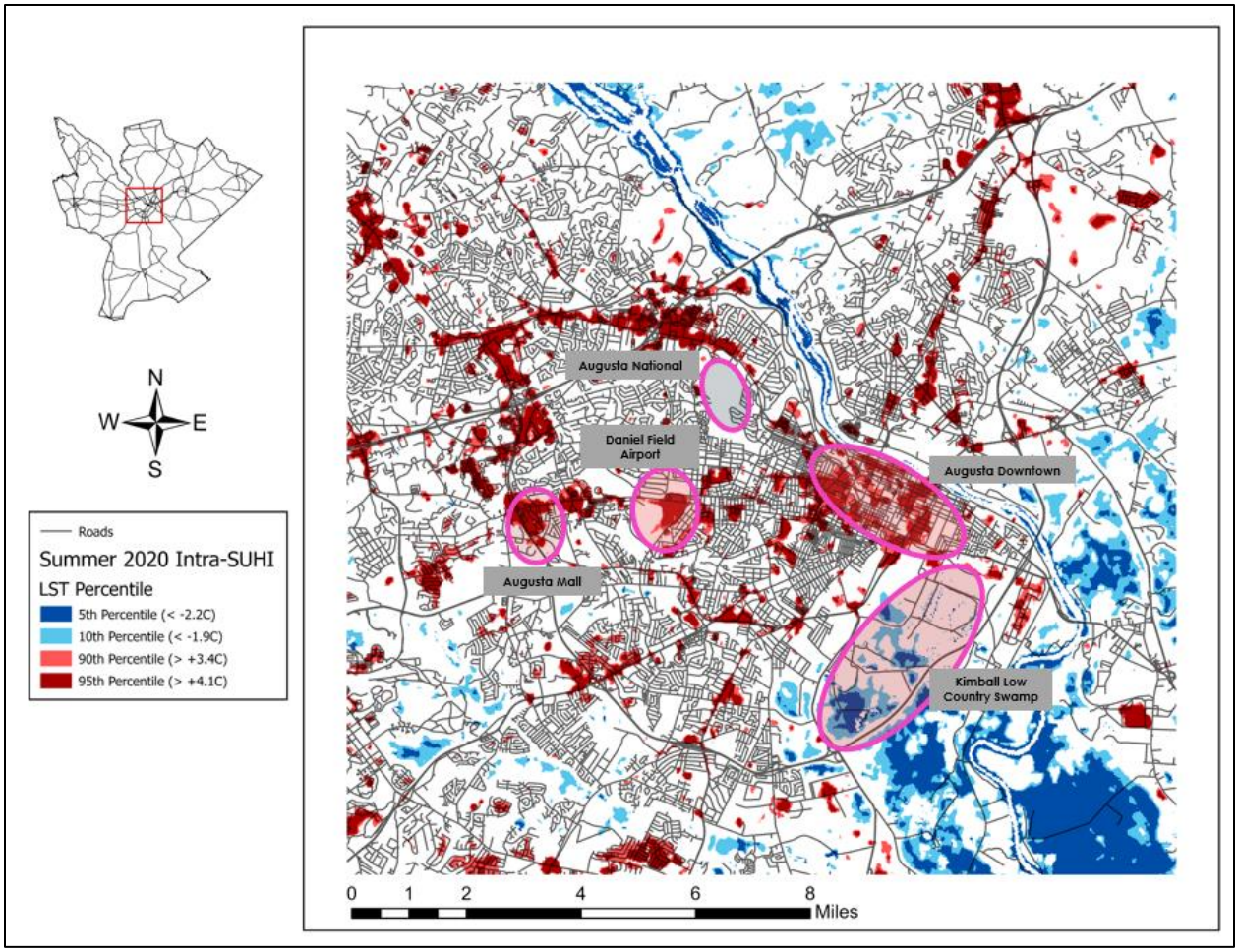

Figure 12. Intra-SUHI for JJA 2020 and 2022 with highlighted points of interest. Data Source: Landsat LST Bundle.

Intra-SUHI to Inform Canopy Layer UHI Data Collection Plans

Visualizing the intra-SUHI anatomy in Augusta is a great aid in delineating a vehicle traverse route and setting preliminary locations for rotary unmanned aerial system (UAS) sounding flights. Layering the intra-SUHI map with 10m resolution visible imagery from Sentinel 2 gives the ability to conduct a comprehensive visual analysis of the study area and select a traverse route that can be driven in under two hours which covers several hot and cold intra-SUHI's and land cover types. The two-hour drive maximum time was chosen in an effort to

minimize temporal bias in the observed spatial patterns of the CLUHI as meteorological conditions evolve throughout the day. By delineating a route in this way, I believe that this can enable a more direct comparison between spatial patterns in the SUHI and the CLUHI if traverse collections can be coordinated with satellite image collections.

Additionally, UAS flight ceiling data from the FAA was added to the layered visible and intra-SUHI map to inform where the UAS will not be limited by altitude restrictions from the nearby Augusta Regional Airport. In uncontrolled airspace, UAS are limited to a maximum altitude of 400 feet (~122 meters) above ground level (AGL) by the FAA, and this ceiling is lowered incrementally with increasing proximity to controlled airspace. Thus, it is ideal to select flight locations outside of altitude restrictions, though exceptions may be made if a desired flight location is within the outermost (highest altitude, 300 feet [~91 meters] AGL) area of UAS ceiling restrictions.

For the CLUHI data collection campaign that was conducted in Summer 2023, a 49.7-mile traverse route was delineated around the urban core of Augusta by following direct routes in-between identified intra-SUHI's (Figure 13). By analyzing the intra-SUHI anatomy along the planned traverse with the FAA UAS ceiling restrictions, I was able to plan eight preliminary flight points that would be verified for accessibility on the first data collection. One of these planned points is located inside of the 300 feet (~91 meters) AGL ceiling restriction around the Augusta Regional Airport, but this was deemed to be acceptable as this point was planned nearby a cold intra-SUHI nearby a swamp and other cold intra-SUHI's were much further into the ceiling restrictions.

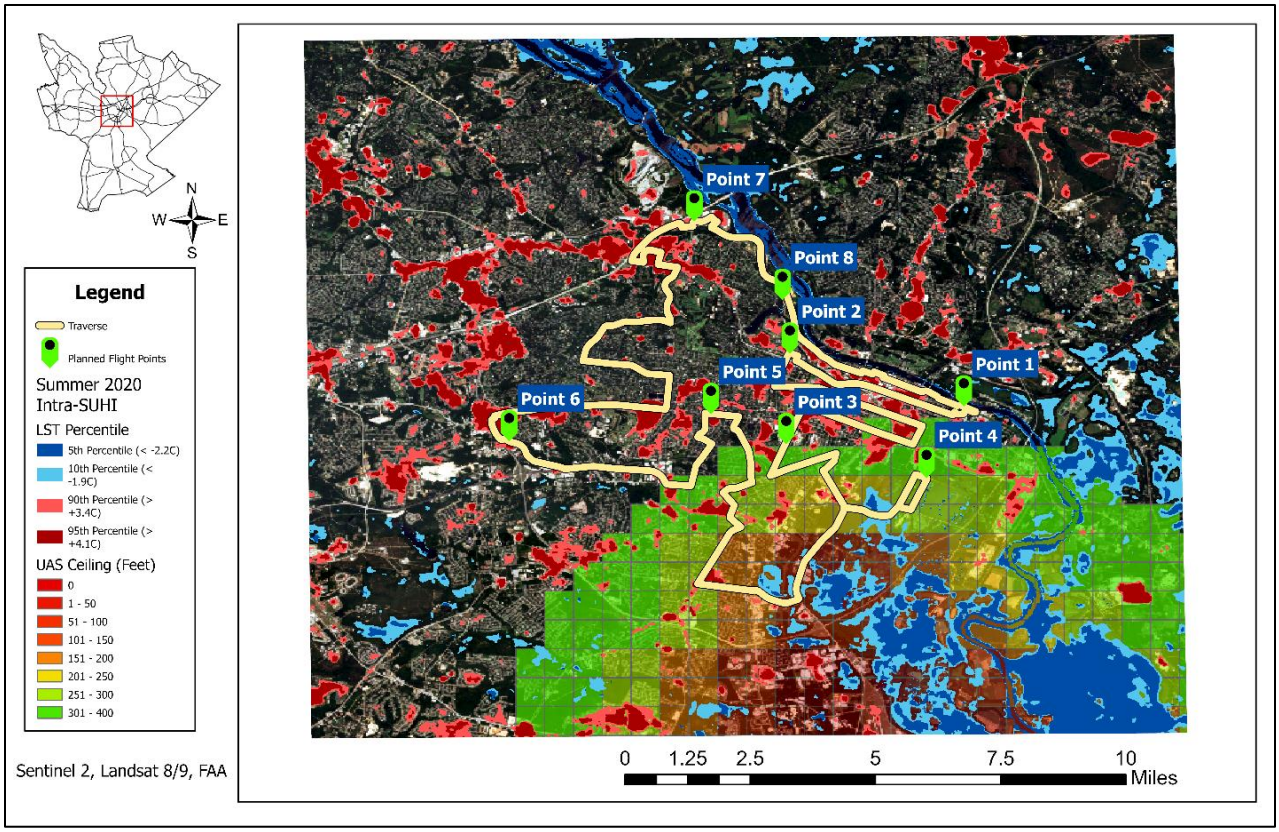

Figure 13. Planned traverse and UAS flight locations, based on visual analysis of the intra-SUHI. Data Source: Landsat LST Bundle, Sentinel 2, FAA

Resultant Canopy Layer UHI Observation Plan

With the aid of the maps presented in the previous sections, and information of Landsat acquisition dates (https://landsat.usgs.gov/landsat_acq), a three-trip, two-person crew CLUHI campaign via vehicle-borne and UAS-mounted low-cost sensors was planned for the summer of 2023. Vehicle-borne and UAS observation equipment is discussed in-depth later in this document. Selecting the trip dates was challenging for a number of factors and required researcher schedule flexibility. For one, Augusta frequently experiences afternoon rainfall in the summer months, and the observation equipment is not waterproof and cannot be used in the rain. Further restrictions were placed on trip date selection by Landsat acquisition dates, with Landsat

8 and 9 having a combined return period of 8 days. Scheduling conflicts with other fieldwork commitments also restricted the dates that would be suitable for data collection. Once all of these factors had been considered and accounted for, the CLUHI observation trips were conducted on July 3-5, August 13-14, and August 20-21, 2023, with Landsat acquisitions on July 4, August 13, and August 21.

In a best-effort attempt to observe the diurnal cycle of heating and cooling, the traverse would be driven four times per day: 7:30AM – 9:30AM, 11:30AM – 1:30PM, 3:30PM – 5:30PM, and 9:00PM – 11:00PM. These specific observation times were chosen to be similar to the observation times by Y. Yin et al. (2020) in their study of the CLUHI and heat exposure in Athens, GA that equipped city buses with similar low-cost sensors. However, their study had the advantage of many data collection vehicles, compared to the single driver that conducted this data collection, and thus they were able to achieve more comprehensive spatial coverage and a near-snapshot temporal resolution. Although meteorological conditions can change within a two-hour time span, this could be worked around by driving the traverse in opposite directions each day of a trip. Additionally, the traverse was planned to be driven at the posted speed limit, typically 35 mph (~56 kph), so as to not impede the natural flow of traffic. Considerations were made in designing the vehicle-borne sensor housing to minimize potential cooling effects of high wind speeds and raise the sensors from the vehicle's boundary layer flow, discussed further in the next chapter of this document.

The first trip, planned for July 3-5, 2023, was designed to be a "shakedown" of the driving traverse route and the vehicle-borne low-cost sensors. This trip was three days, as opposed to two days for trips two and three, due to the July 4th Independence Day celebrations and the associated risks to driver safety disallowing data collections in the afternoon and night.

During this trip, the driver was to get acquainted with the study area and the traverse plan, as well as scope out and verify the accessibility of planned locations for UAS data collection flights to be conducted during trips two and three.

Trips two and three were planned to feature the same traverse collection methods, as well as collect UAS observations of the vertical structure of the CLUHI up to the FAA-mandated 400-foot (~122 meter) ceiling on day two of trips two and three. The primary purpose of these flights is to devise methods for, and demonstrate the feasibility of, UAS observations in an urban environment and the value of low-cost sensors for meteorological data collection. The UAS pilot would fly each of the eight planned flights points twice during the observation day, beginning around 9:30 AM – 10:00 AM and finishing around 7:00 PM – 7:30 PM, while driving the most direct route between points. The UAS pilot's vehicle was not equipped with observation equipment. The UAS utilized for this study, a DJI Matrice 600 Pro, was equipped with identical low-cost sensors to the collection vehicle, as well as a FLIR Duo R radiometric thermal imager to capture LST at flight points. Special considerations were made when designing and mounting the UAS-mounted low-cost sensor housing to minimize potential cooling effects of rotor wash, discussed further in the next chapter of this document.

This field plan was devised as a best-effort to maximize the amount of data that could be collected with just a two-person field crew on a limited budget. Having just one driver and just one UAS pilot presents considerable challenges to temporal continuity within the data. For the traverse CLUHI data collections, this issue can be minimized by driving the traverse in opposite directions on each day of collection. This challenge is more difficult to address with the UAS, as only one single location can be observed with one single UAS pilot. However, as this study aims more to evaluate the feasibility of UAS in an urban environment and does not yet intend to

provide a comprehensive analysis of the spatial and temporal patterns of CLUHI vertical structure, the temporal offsets between the flights are not a major issue with the scope of this project.

CHAPTER 5

LOW-COST SENSOR DEVELOPMENT

Sensor Selection

In order to equip both the collection vehicle and the rotary UAS with identical sensors, it was not possible to purchase off-the-shelf products such as the highly regarded iMet XQ2 (Inoue & Sato, 2022; Samad et al., 2022; Varentsov et al., 2023) or Trisonica Mini (Greenfield & Thaxton, 2022; Samad et al., 2022). Therefore, a low-cost Arduino-based setup provided the best option available to this study.

At least two recent studies have explored the use of such a system and showed good quality measurements (Chang et al., 2020; Chodorek et al., 2021), and to keep this study in line with current literature, the sensors were selected from those used in the two mentioned studies. Chodorek et al. explored the Bosch Sensortec BME280 (measures temperature, relative humidity, and atmospheric pressure) and the MEAS HTU21D (measures temperature and relative humidity), and Chang et al. explored the BME280 and the Sensirion SHT31-D (measures temperature and relative humidity). Both of these studies found that all three of the sensors perform well when calibrated with a trusted weather station, but that the BME280 is slightly inferior to the other sensors for temperature accuracy and recommend using it primarily for pressure readings. Both studies also recommend that similar sensor systems should be similarly calibrated to a trusted weather station to verify their accuracy.

To keep in line with the two studies discussed above, the BME280 sensor was chosen to provide primary pressure measurements and secondary temperature and relative humidity

measurements. This then left a choice between the HTU21D and the SHT31-D. However, the choice was made easy by the fact that the HTU21D sensor was unavailable from all suppliers at the time of design and construction, therefore the SHT31-D was chosen as the primary temperature and relative humidity sensor. Both the BME280 and SHT31-D were sourced from Adafruit Industries (https://www.adafruit.com/) and are a part of their plug-and-play STEMMA QT / Qwiic breakout board system (https://www.adafruit.com/category/1005). Additionally available from Adafruit was the brand new Sensirion SHT45 (measures temperature and relative humidity), a new evolution of the SHT31-D that claims higher accuracy than the older construction. Searches were unable to find any studies that had tested the new SHT45 for atmospheric observations, so this was also selected to test against the proven SHT31-D, but no expectations were set for its usability and the data would be ignored if there is low confidence in its quality. The selected sensors and the manufacturer's claimed accuracies are presented below in Table 1.

Table 1. Summary of selected sensor claimed accuracy.

Sensor	Temperature Accuracy	Humidity Accuracy	Pressure Accuracy
BME280	± 1ºC (-45ºC-85ºC)	± 3% (20%-80%)	± 1 hPa (300hPa-1100hPa)
SHT31-D	± 0.3ºC (-40ºC-125ºC)	± 2% (0%-100%)	n/a
SHT45	± 0.1ºC (0ºC-75ºC)	± 1% (0%-100%)	n/a

Sensor Unit Control Hardware and Testing

The Adafruit Feather (https://www.adafruit.com/category/943) line of microcontroller main boards (Feathers) and stackable accessory boards (Wings) was chosen as the foundation of

the sensor unit for its wide range of microcontroller options and very user-friendly design. The Raspberry Pi RP2040 Feather, programmed with Arduino, is very popular with hobbyists for its versatility and has lots of community support for learning, therefore the RP2040 was chosen as the microcontroller for the sensor unit. Two Wings were added to the RP2040 Feather: the Adalogger FeatherWing to record observations, and the Adafruit Ultimate GPS FeatherWing to record geographic location and record the time from GPS satellites. The Adalogger also contains a real-time clock that is set automatically when the microcontroller is programmed, but this is subject to drift and is not reliable, therefore the GPS time was used in data collection. A 512mb microSD card was chosen to record the data, and both the Adalogger and Ultimate GPS FeatherWings were equipped with a CR1220 backup battery to keep time even while the microcontroller is turned off. Additional hardware for the sensor unit were three STEMMA QT/Qwiic JST SH 4-pin cables to daisy-chain the sensors together and plug into the RP2040 Feather, as well as a 3.7V, 500 mAh lithium-ion polymer (Li-Po) battery. Altogether, the total cost per assembled sensor unit was $103.00, summarized in Table 2 and presented in Figure 14. Components for three sensor units were purchased, with one unit being for backup and testing, one unit to be deployed on the data collection vehicle, and one to be deployed on the rotary UAS for a total three-unit purchase price of just $309.00.

Table 2. Summary of sensor unit hardware and cost

Quantity	Item	Unit Price
1	Bosch Sensortec BME280	$14.95
1	Sensirion SHT45	$12.50
1	Sensirion SHT31	$13.95
1	Adafruit Feather RP2040	$11.95
1	Adalogger FeaterWing	$8.95
1	Ultimate GPS FeatherWing	$24.95
1	3.7V, 500 mAh Li-Po Battery	$7.95
3	50mm STEMMA QT Cable	$0.95
1	512mb microSD Card	$4.95

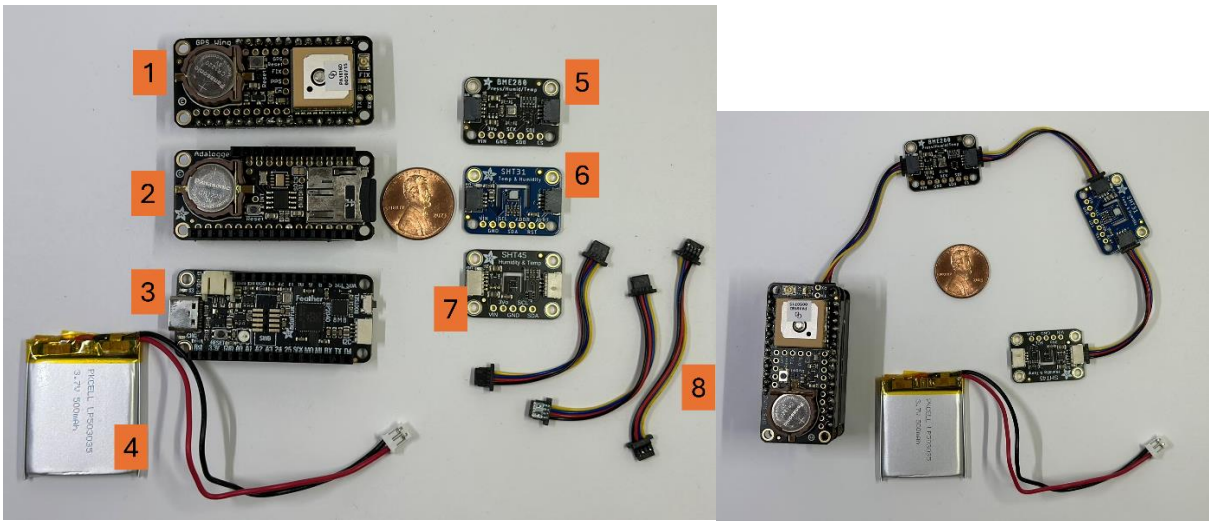

Figure 14. Disassembled (left) and assembled sensor unit (right), penny for scale. Labels: 1. Ultimate GPS FeatherWing; 2. Adalogger with 512mb microSD card; 3. Feather RP2040; 4. 3.7V, 500mAh Li-Po battery; 5. Sensirion SHT45; 6. Sensirion SHT31-D; 7. Bosch Sensortec BME280; 8. Three STEMMA QT/Qwiic JST SHT 4-pin cables.

Sensor Calibration and Correction

Due to time constraints leading up to and between the three field collections, the sensors were not able to be compared against a trusted weather station before deployment, and any corrections would need to be applied post-hoc to the raw data prior to conducting any data analysis. Very soon after the final field collection, the three sets low-cost sensors were set alongside the Davis Instruments weather station on the rooftop garden of the geography building at University of Georgia to record temperature, pressure, and relative humidity data for a period of 3 hours from 1:00 PM – 4:00 PM on August 17, 2023, at a sampling rate of 1 Hz. The conditions of the measurement period were similar to conditions when the sensors were deployed, with a weather station-measured temperature range of 29.1°C – 30.9°C and relative humidity range of 45% - 57%.

This calibration test revealed worse-than-advertised sensor performance in raw data across all three selected sensors for temperature and relative humidity in the daisy-chain setup used here, and especially poor for the SHT45, summarized in Table 3. Only the pressure measurements from the BME280 required zero correction, with an observed mean absolute error (MEA) of 0.77 hPa and root mean square error (RMSE) of 0.85 hPa from the weather station's observations over the calibration period.

Table 3. MEA and RMSE for temperature (°C) and relative humidity (%) low-cost sensor calibration measurements.

Sensor	Temperature MAE	Temperature RMSE	RH MAE	RH RMSE
bme	1.08	1.24	14.54	14.64
sht31	1.09	1.19	8.59	8.74
sht45	2.32	2.37	17.71	17.79

The SHT45 showed the worst performance of all three sensors, and this was also the last sensor in the STEMMA QT/Qwiic daisy chain of sensors. This leads me to hypothesize that there may be signal interference or voltage fluctuations from the sensors as the measurement signal is sent through the daisy-chained sensors to the microcontroller. However, although the BME280 showed the most accurate temperature readings, it showed relative humidity readings that were well outside of its claimed accuracy of ±3%. Prior to future deployments of the sensor units, the sensors will be tested individually to test if the daisy-chain construction has an effect on the measurement accuracy. If results from this test show better sensor performance if only one is used at a time, the daisy-chain construction method and/or sensor location within the chain will likely need to be re-evaluated.

Although there are very apparent discrepancies between the sensor measurements and weather station measurements, fitting an ordinary least squares (OLS) linear regression model to the raw data was able to bring observations to comparable levels of accuracy. OLS models were fitted for temperature and relative humidity for each of the three sensors, a two-sensor mean with observations from the BME280 and the SHT31-D, and a three-sensor mean with all sensor observations. Additionally, two-second rolling means of the temperature and relative humidity observations were calculated and fitted with OLS models. Of the tested calibration models, the 1 Hz two-sensor mean showed the best performance for both temperature and relative humidity with residual standard deviations of 0.24°C and 1.6%, respectively, at the 95th percentile confidence level ($p < 0.05$). Calculating the MEA and RMSE again on the two-sensor mean model-corrected data yielded satisfactory results. Corrected temperature measurements showed a MAE of 0.2°C and RMSE of 0.25°C, and corrected relative humidity measurements showed a MAE of 1.28% and RMSE of 1.56%.

Chang et al. (2020) note and provide a correction formula for a delayed temperature response compared to pressure and relative humidity observations in the BME280 due to its construction as a bandgap temperature sensor, and this was observed in the raw data gathered during a test flight with the UAS. However, this technique of OLS regression with a two-sensor mean had the unintended effect of eliminating this lag, thereby simplifying the data analysis.

While post-hoc sensor calibration as conducted here is not typically standard practice, it was unfortunately the only option available to this study. By comparing the low-cost sensors to a trusted weather station, the results from the calibration test give confidence that applying the OLS calibration models to the raw two-sensor mean for temperature and relative humidity provides consistent and reliable observations that are trustworthy for analysis.

Custom Sensor Housings

Working with a low budget and limited time meant that a lot of DIY creativity was required to design and build custom housings to mount on both the ground vehicle and the UAS. All of the prototyping and final designs made use of spare materials from either the author's lab's supply closet or from the author's home workshop. Only common tools that are typically found in a moderately-equipped home workshop were necessary to construct these housings.

Careful design considerations had to be taken for both mounts to minimize wind effects on the measurements. For the ground vehicle sensor unit (VSU), the sensors had to be shielded from head-on winds and buffeting, shielded from direct solar radiation, elevated away from the collection vehicle's boundary layer flow while driving, and the GPS unit required an open sky view to measure location as accurately as possible. For the UAS (drone) sensor unit (DSU), the sensors had to be isolated from any radiant heat from the UAS body and shielded from rotor wash.

To address these challenges for the VSU (Figures 15 - 17), a 12” section of 3” inner-diameter Schedule 40 PVC tube was used as the outer shell and would be mounted laterally on the vehicle with the long side facing the direction of travel and the openings of the tube perpendicular to the direction of travel. A custom protective box to keep the microcontroller stack and battery as a unit was 3D printed. The sensors and microcontroller box were mounted with plastic zip ties to a 12” x 2” x 0.5” wood plank that slid into the PVC tube and also attached with plastic zip ties. The sensors centered on the plank to isolate them from wind buffeting as much as possible, and a power switch was soldered in and attached to the plank also with a plastic zip tie. To ensure sufficient sky view for the GPS receiver, a small 1” x 1” square was cut out of the top of the PVC tube. While deployed in the field on the collection vehicle, the VSU was attached with plastic zip ties to the flat side of a 13” x 13” x 11” milk crate, which was attached also with plastic zip ties to the top of a metal frame roof rack that is hard mounted to the vehicle. In total, this gave approximately 18” of elevation above the vehicle’s rooftop (Figure 18).

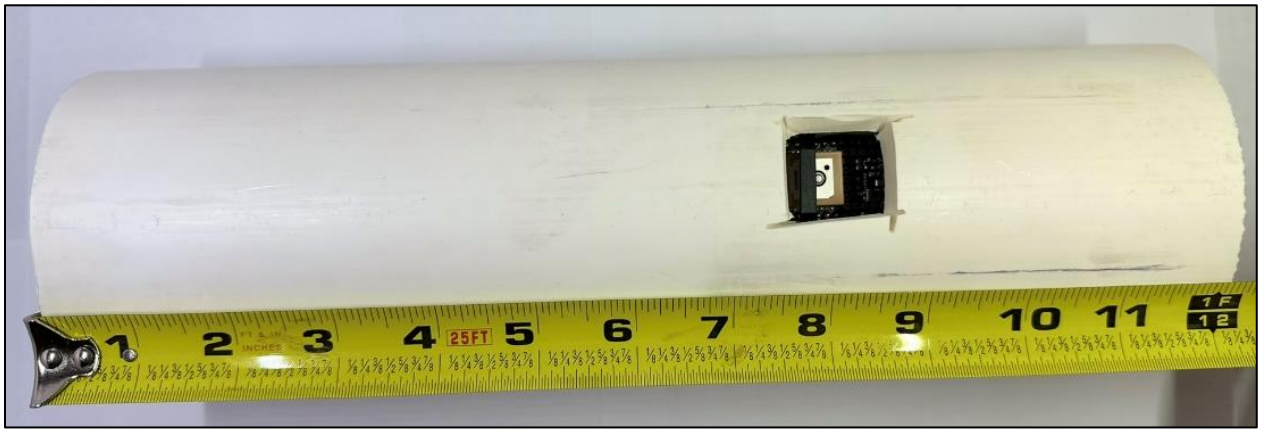

Figure 15. Assembled VSU. The GPS receiver is visible through the top.

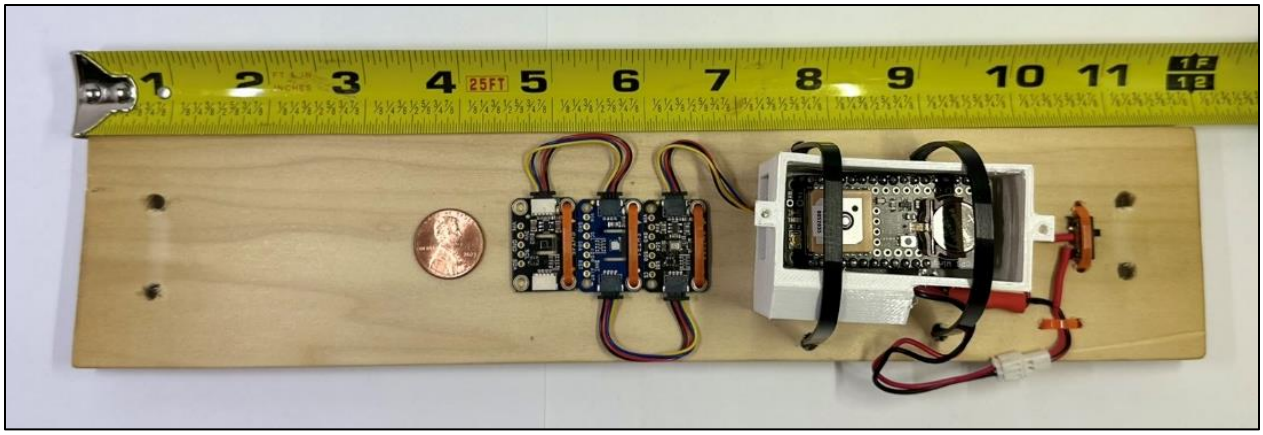

Figure 16. VSU inner plank layout with power switch on the right. Penny for scale.

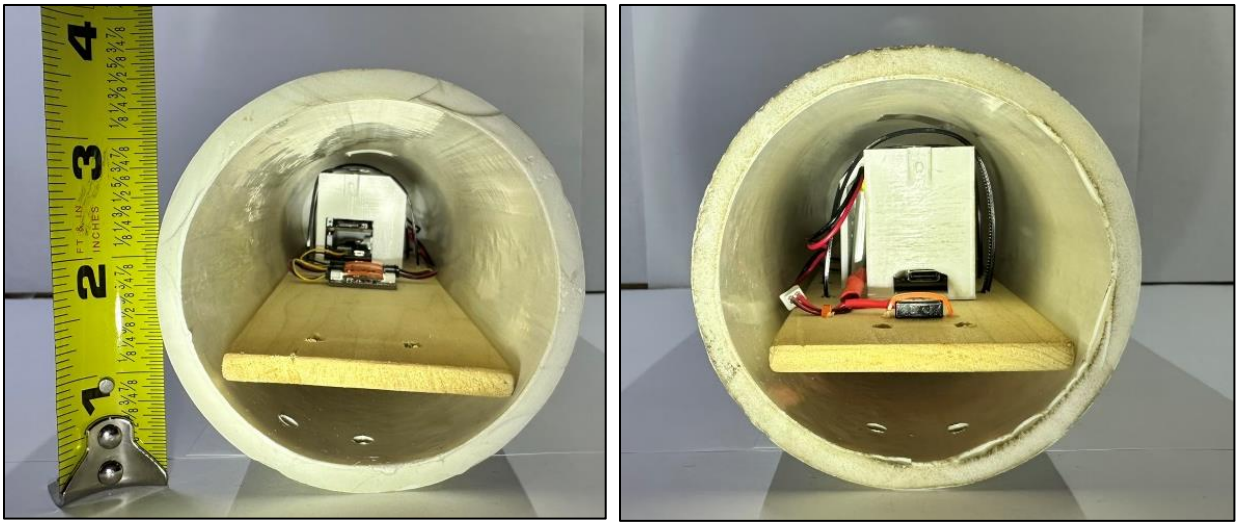

Figure 17. Left and right side views of the assembled VSU.

Figure 18. Collection vehicle equipped with the VSU (red circle).

Designing and building the DSU proved to be more challenging than the VSU. The sensors had to attach the UAS in such a way to be away from rotor wash, but that it would not have to be detached when ferrying the UAS between flight points. Existing literature suggests a choice between one of two courses of action for sensor placement on a UAS. One option is to place the sensors on a pole that attaches to the top of the UAS body and stays away from any and all rotor wash (Greenfield & Thaxton, 2022; Samad et al., 2022), but this has the drawback of needing to be removed for transport in a vehicle. The other option is to place the sensors somewhere below the UAS body, either on one of the UAS legs (Chang et al., 2020; Varentsov et al., 2022) or directly underneath the body (Chodorek et al., 2021). The UAS that was available for this study was a DJI Matrice 600 Pro courtesy the Disruptive Geospatial Technologies Laboratory at the University of Georgia, and is equipped with retractable landing gear, meaning

that leg-mounting was not an option. Therefore, the DSU would be mounted directly underneath the body and the housing would be designed with that placement in mind.

The DSU (Figures 19 - 23) was based on a weather station temperature sensor plate solar radiation shield. The solar radiation shield was disassembled plate-by-plate and the whole unit was shortened. Three plates of the shield were retained and specially adapted to host the sensors and microcontroller stack. To create gaps between plates and act as a shock absorber for in-flight vibrations, 1/4” inner-diameter rubber tubing was cut to size and placed between the plates. A small USB-C fan and portable battery pack were mounted to provide active ventilation to the sensors, and a piece of corrugated cardboard was used as a spacer and shock absorber between the portable battery and the bottom of the modified radiation shield. The modified radiation shield was bolted to an 8” x 4” x 0.5” plank that had holes drilled to attach to rails on the underside of the UAS with plastic zip ties. A power switch was also added to the DSU following system glitches encountered during the first attempt at data collection.

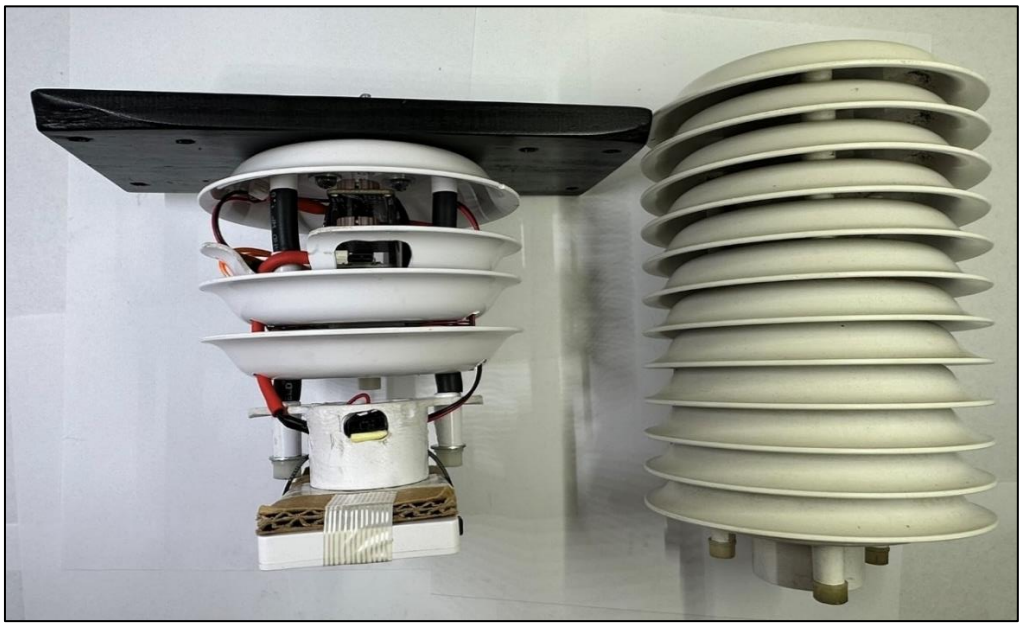

Figure 19. Assembled DSU alongside base radiation shield.

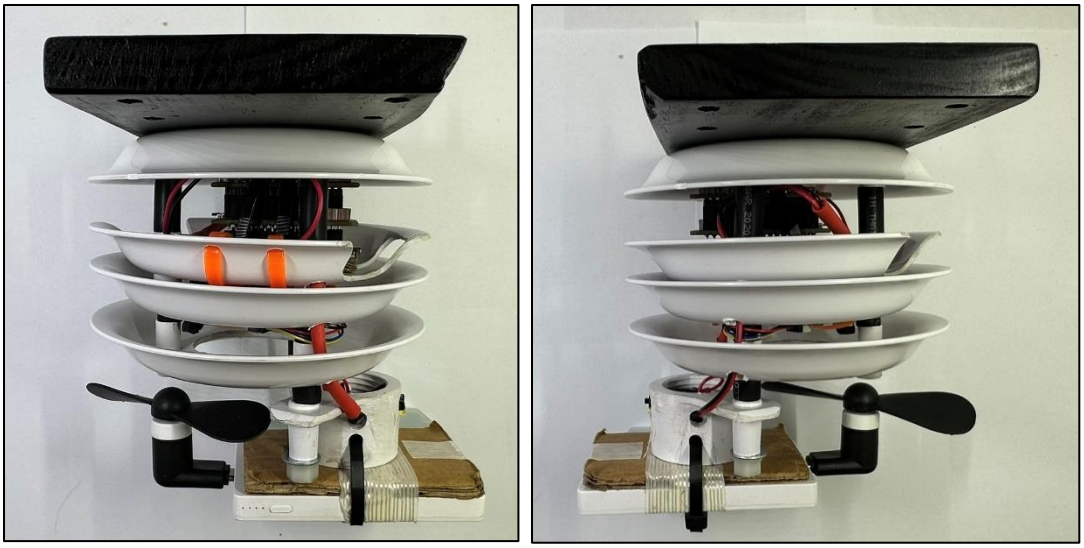

Figure 20. Side views of the assembled DSU.

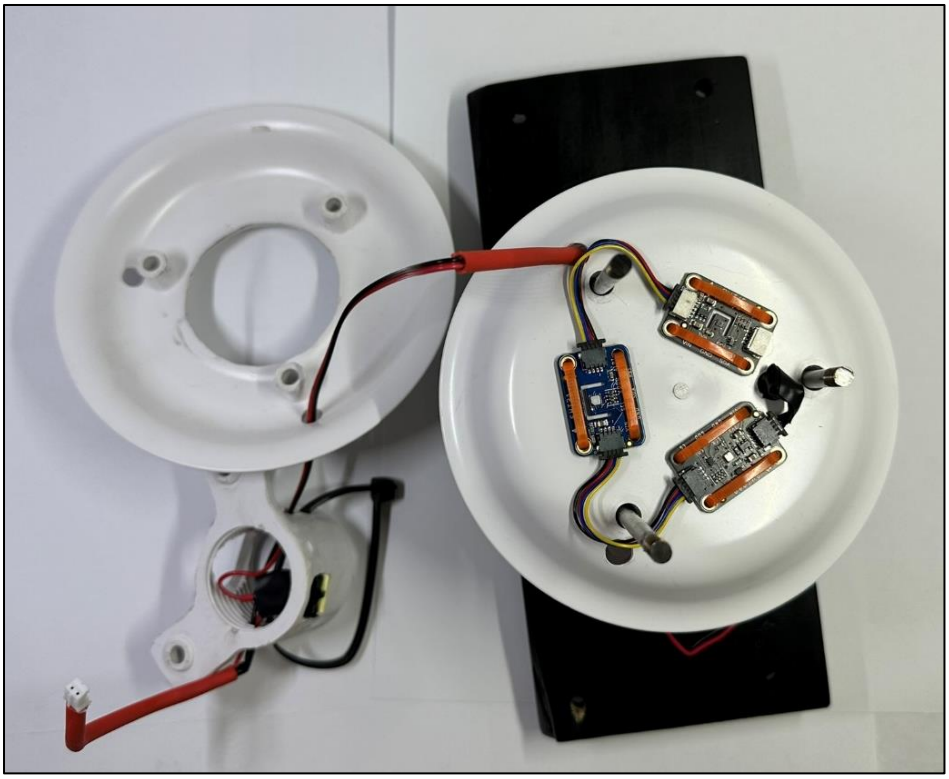

Figure 21. Bottom view of partially disassembled DSU. Bottom plate removed to reveal sensor placement. Active ventilation is provided through the large hole in the bottom plate.

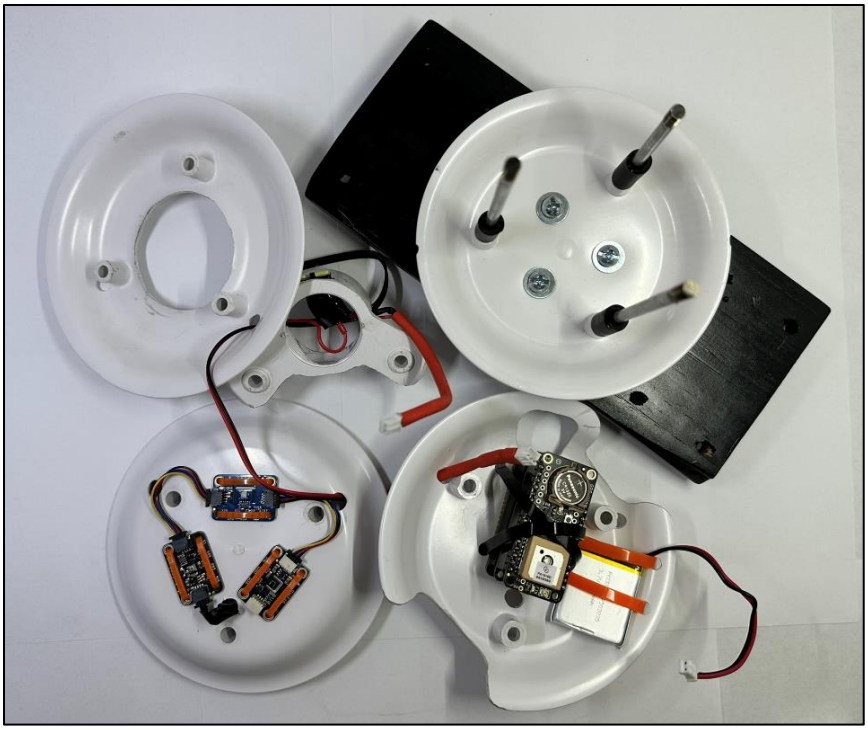

Figure 22. Fully disassembled DSU revealing placement of the microcontroller stack and battery, as well as how it is attached to the wood plank.

Figure 23. DJI Matrice 600 Pro equipped with the DSU (yellow circle).

CHAPTER 6

SUMMER 2023 DATA COLLECTION CAMPAIGN REPORT

This chapter provides a brief summary of events for each trip of the Summer 2023 CLUHI data collection campaign, as well as daily temperature departures from the 1981-2010 monthly mean at the Augusta Daniel Field airport. Weather data was acquired from the National Centers for Environmental Information online Local Climatological Data tool (https://www.ncdc.noaa.gov/cdo-web/datatools/lcd).

Trip 1: July 3-5, 2023

The first trip of the CLUHI data collection campaign was conducted between July 3-5, 2023, aligning with the Landsat acquisition on July 4. This trip was designed to be a shakedown of the low-cost sensors in the VSU and the drivability of the traverse route. There were no UAS flights planned or conducted on trip 1. On days one and three of the trip, the plan was to drive the traverse at all four planned collection times (7:30AM – 9:30AM [morning], 11:30AM – 1:30PM [midday], 3:30PM – 5:30PM [afternoon], and 9:00PM – 11:00PM [night]). Day two collections were restricted to just the morning and midday drives due to driver safety concerns as July 4th celebrations began in the afternoon. Unfortunately, the afternoon and night collections on day three of the trip also had to be cancelled due to rain in the study area.

From 1981-2010, the climatological average July minimum, maximum, and average air temperature observed at the Augusta Daniel Field airport (KDNL) is 22.4°C, 33.2°C, and 27.8°C, respectively. For July of 2023, the daily minimum, maximum, and average air temperatures were 23.4°C, 33.8°C, and 28.6°C, respectively. On average, July 2023 was 0.8°C

warmer than the 1981-2010 average. On day 1 (July 3, 2023), the average temperature was 28.3°C, the average temperature for day 2 (July 4, 2023) was 30°C, and the average temperature for day 3 (July 5, 2023) was 28.9°C. The departure from the 1981-2010 monthly means were +0.5°C, +2.2°C, and +1.1°C for days 1, 2 and 3, respectively.

Trip 2: August 13-14, 2023

The second trip of the CLUHI data collection campaign was conducted between August 13-14, 2023, aligning with the Landsat acquisition on August 13. The original plan for collection times was to collect at all four planned times, but unplanned illness on both mornings meant that the driver was unable to go out for collection in the mornings. Data collection was successfully carried out for the midday, afternoon, and night times on both days. The traverse was driven clockwise on day one and counterclockwise on day two.

This trip was also planned to be the first data collection with the UAS on August 13, but a system glitch in how the DSU was powered on (maneuvering the battery cable to plug into the microcontroller in a very tight space) meant that no meteorological observations were collected by the UAS during trip two. Thermal images were still captured, though these were not utilized for analysis. To correct the DSU issues before the third trip, a power switch was added to the DSU, and a flashing light signal was programmed to only flash while data was being recorded. This completely fixed the issue and made the DSU much more user-friendly.

From 1981-2010, the climatological average August minimum, maximum, and average air temperature observed at the Augusta Daniel Field airport (KDNL) is 22°C, 32.2°C, and 27.1°C, respectively. For August of 2023, the daily minimum, maximum, and average air temperatures were 23.1°C, 33.8°C, and 28.4°C, respectively. On average, August 2023 was 1.3°C warmer than the 1981-2010 average. On day 1 (August 13, 2023), the average temperature

was 28.9°C and the average temperature for day 2 (August 14, 2023) was 31.1°C. The departure from the 1981-2010 monthly means were +1.8°C and +4°C for days 1 and 2, respectively.

Trip 3: August 20-21, 2023

The third trip of the CLUHI data collection campaign was conducted between August 20-21, 2023, aligning with the Landsat acquisition on August 21. This trip went fully to plan, and the traverse was driven during all four planned collection times on both days of the trip. The traverse was driven counterclockwise on day one and clockwise on day two.

The UAS and pilot were available on August 20, and meteorological data was successfully recorded by the DSU. Flight point 6 was the closest point to the origin of the UAS pilot (Athens, GA), and the flight rounds started here and continued to point 5, then point 4, and so on until all of the points had been flown twice. Flying the points in this direction coincided with the counterclockwise direction of travel along the traverse on that day. Flight point 7 was the last to be reached before the UAS pilot would merge onto the interstate to return to Athens, GA, so this point was able to be flown three times. Flight point 4 had to be moved between the first and second flight due to a misunderstanding on what was public vs. private land, but the move was just across the street.

On day 1 (August 20, 2023), the average temperature was 29.4°C and the average temperature for day 2 (August 21, 2023) was 30.6°C. The departure from the 1981-2010 monthly means were +2.3°C and +3.5°C for days 1 and 2, respectively.

CHAPTER 7

SUMMER 2023 ANALYSIS AND RESULTS

This chapter describes the methodology and results of a comprehensive analysis of urban heat patterns for the summer of 2023 as observed by satellite remote sensing and in-situ data collection via ground vehicle-borne and UAS-based sensors. Possible implications of these findings are discussed further in the Chapter 8.

Surface UHI and Land Cover Relationships

Applying the remote sensing methodology for SUHI observation described in Chapter 3, sections 1 – 3, to investigate the SUHI and intra-SUHI's in Augusta for JJA 2023 revealed similar spatial patterns of hot and cool areas as the SUHI and intra-SUHI maps used for CLUHI observation planning of JJA 2020/2022. However, JJA 2023 exhibited higher peak SUHI intensity than the first observations (Figure 24), approximately 9ºC higher than for JJA 2020/2022. Additionally, the 90^{th} and 95^{th} percentile intra-SUHI thresholds increased by 7.6ºC and 11.2ºC, respectively.

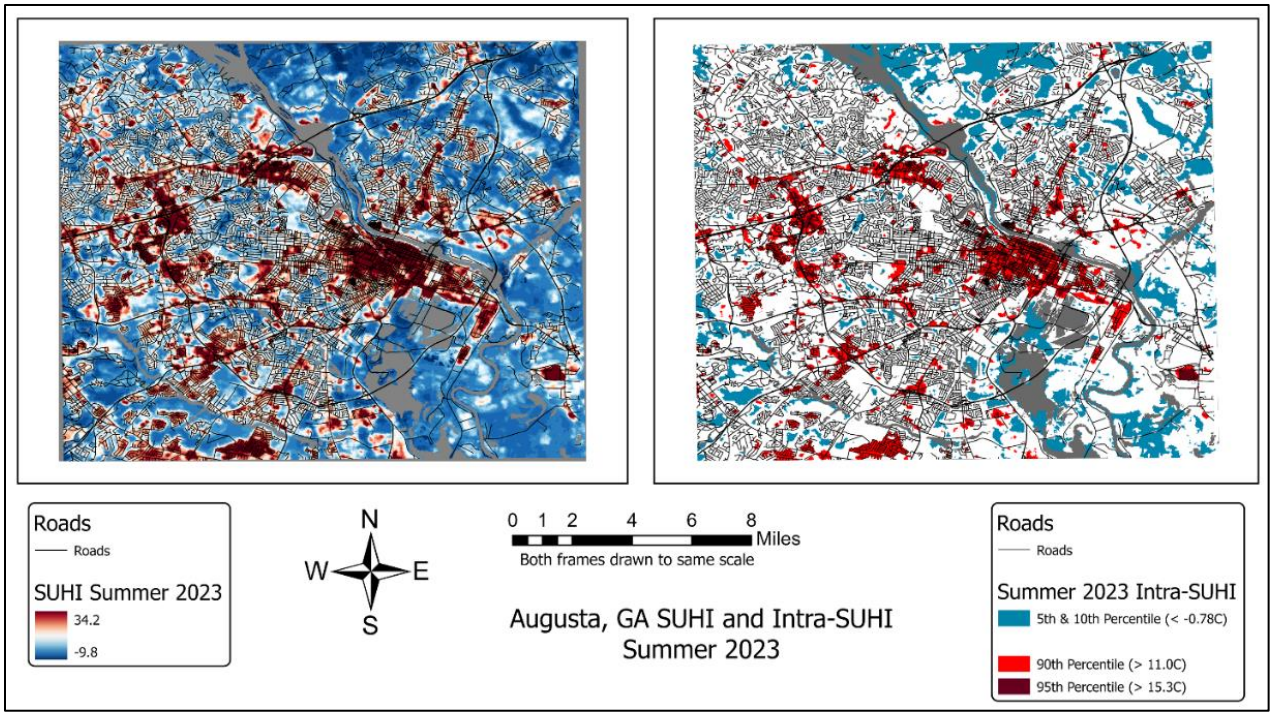

Figure 24. Observed SUHI intensity and intra-SUHI's, JJA 2023

Further investigation into the results showed that the peak SUHI intensity of 34.1°C and its closest neighbors represented an extreme outlier that skewed the data. This outlier corresponds to a large manufacturing plant owned by the Kimberly-Clark Corporation, though exhaustive searches were unable to reveal the industrial activities that take place there. Removing this feature from the data set reduced peak SUHI intensity as well as the 90th and 95th percentile intra-SUHI thresholds, but both were still elevated from the JJA 2020 results (Figure 25). It seems the most likely explanation for this was that industrial activity at the Kimberly-Clark facility and other industrial centers was greatly reduced or even ceased during the summer of 2020 due to the global impacts of the COVID-19 pandemic that began in the US in March 2020. This would reflect findings of reduced urban heat islands in over 300 megacities in China during the COVID-19 lockdowns that were implemented in the country (Liu et al., 2022). There

are several industrial areas around Augusta, and it is possible that production ramping up between 2020 and 2023 also increased their LST signature, thus increasing overall SUHI intensity.

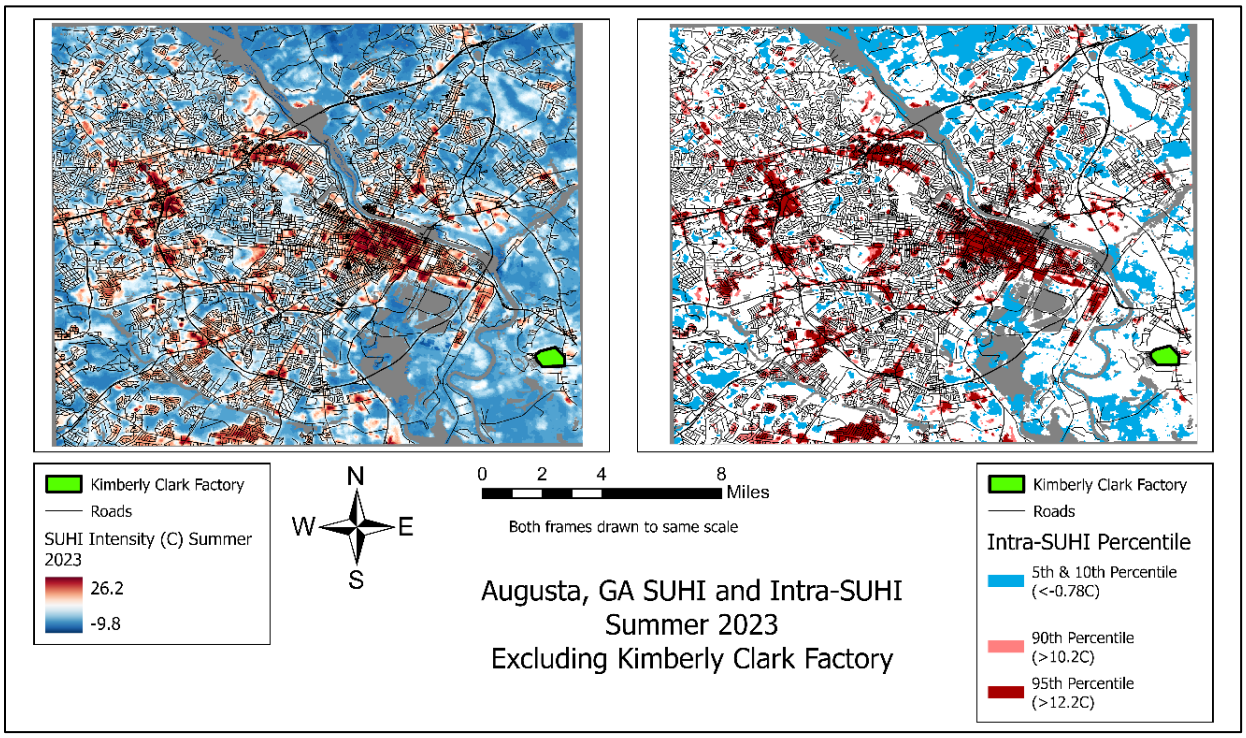

Figure 25. Observed SUHI intensity and intra-SUHI's with Kimberly-Clark Factory masked from the results, JJA 2023.

From the JJA 2023 SUHI observations, two sets of 500 random sample points of LST, NDVI, percent tree cover (TC), percent impervious surface (Imp), and NLCD classification were created within the urban core study area and within the area of the MSA that is covered by the single Landsat image footprint used for JJA 2023 analysis (Figure 26). All observations were sampled together at the same two sets of 500 points. With these sample sets, statistical analysis via Pearson correlation coefficients and OLS regression models, described in Chapter 3, section

4, were conducted to investigate the relationship between the land surface temperature (for June, July, August, and JJA mean) and land cover variables in Augusta.

Figure 26. Map of single Landsat scene coverage. Random sample points were generated only within the image area.

Pearson correlations for the city study area reveal moderate-to-high correlations between LST and the tested variables (TC, Imp, and NDVI) (Table 4). TC and NDVI showed negative correlations with LST, and Imp showed positive correlations. The correlations of LST with Imp and NDVI are essentially equal in magnitude, but opposite in sign. Within the city study area, TC's correlations were slightly lower magnitude than for Imp and NDVI, but good correlation is still observed across each month and all JJA. OLS regression model statistics showed slight-to-moderate relationships between LST and the tested predictor variables (NLCD, NDVI, TC, Imp,

TC+Imp) with *p*-values < 0.05 for all OLS models (Table 5). The TC-only model showed the lowest performance, with an adjusted R^2 value of 0.368 and residual standard deviation (RSD) of 3.456°C in the model. The categorical NLCD model showed the best performance within the city (adj. R^2 = 0.596, RSD = 2.764), but this model is limited by the fact that it does not reveal what this means for each individual NLCD category, just that a relationship does exist. However, analyzing this against the Pearson correlation coefficients suggests that "Developed" categories have a positive relation with LST, and that natural land cover categories (ex. forests or fields) have a negative relation with LST. The bivariate Imp+TC model showed the next highest performance (adj. R^2 = 0.559, RSD = 2.886°C). It is possible that other linear regression models could reveal greater insight into any possible cross correlations, though this was not tested by this study and may be explored further in future studies.

Table 4. Pearson correlation coefficients for LST and tested variables in the city study area, JJA 2023.

Pearson Correlation, City Study Area

n = 500

Parameter[1]	TreeCover	Imperv	NDVI_Month[2]
LST_June	−0.574	0.681	−0.654
LST_July	−0.620	0.678	−0.682
LST_Aug	−0.632	0.699	−0.713
LST_JJA	−0.608	0.714	−0.647

[1] Correlation based on mean LST observation values for the observation period indicated (monthly mean or JJA mean).

[2] NDVI for observation period indicated by LST variable (monthly mean or JJA mean).

Table 5. OLS regression model statistics for LST with the predictor variables in the city study area, JJA 2023.

OLS Regression Model Statistics, City Study Area

n = 500, Parameter: LST

Model	R-squared	Adjusted R-squared	Resid. St.Dev	P-value
Cty_nlcd	0.608	0.596	2.764	< 0.05
Cty_ndvi	0.419	0.418	3.318	< 0.05
Cty_tc	0.369	0.368	3.456	< 0.05
Cty_imp	0.510	0.509	3.047	< 0.05
Cty_tc_imp	0.561	0.559	2.886	< 0.05

NDVI regression based on mean NDVI for JJA.

When applied to the random sample data from the whole MSA, Pearson correlations show the same positive (Imp) and negative (TC and NDVI) relationships to LST (Table 6). However, the magnitude of correlation with Imp decreased to only slight-to-moderate positive correlation with LST while NDVI increased to high correlation with LST. This likely is due to there being a higher concentration of Imp and lower concentration of vegetation (including non-tree vegetation) within the city study area than in MSA as a whole, making it more likely for the 500 points to be generated away from developed areas in the MSA sample. OLS regressions showed weaker, but still moderate model performance ($p < 0.05$) across the board of tested predictors (Table 7). For the MSA, the NDVI-only regression model showed the highest adjusted R^2 value (0.485) but showed the largest RSD (3.810°C). The bivariate Imp+TC model showed the next highest performance in adjusted R^2 (0.453) and the lowest RSD (2.707°C). The Imp-only model showed the weakest performance (adj. R^2 = 0.220, RSD = 3.235°C), which is in line with the lower correlations with Imp in the MSA compared to the city study area.

Table 6. Pearson correlation coefficients for LST and tested variables in the MSA study area, JJA 2023.

Pearson Correlation, Full MSA n = 500			
Parameter[1]	TreeCover	Imperv	NDVI_Month[2]
LST_June	−0.617	0.459	−0.775
LST_July	−0.604	0.360	−0.823
LST_Aug	−0.554	0.485	−0.745
LST_JJA	−0.611	0.471	−0.714

[1] Correlation based on mean LST observation values for the observation period indicated (monthly mean or JJA mean).

[2] NDVI for observation period indicated by LST variable (monthly mean or JJA mean).

Table 7. OLS regression model statistics for LST with the predictor variables in the MSA study area, JJA 2023.

OLS Regression Model Statistics, Full MSA n = 500, Parameter: LST				
Model	R-squared	Adjusted R-squared	Resid. St.Dev	P-value
MSA_nlcd	0.421	0.398	2.840	< 0.05
MSA_ndvi	0.509	0.485	3.810	< 0.05
MSA_tc	0.373	0.371	2.904	< 0.05
MSA_imp	0.222	0.220	3.235	< 0.05
MSA_tc_imp	0.457	0.453	2.707	< 0.05

NDVI regression based on mean NDVI for JJA.

Comparing the evaluations of the two samples with the differences in correlation and model performance of LST for natural land cover variables vs. developed land cover variables, and that the bivariate TC+Imp OLS regression showed good performance for both random sample datasets suggest that more complex relationships between LST and land cover exist than

are explored here. It is also possible that correlations between land cover and LST may vary by time of day and solar angle, though observations with a much higher temporal resolution than can be offered by Landsat would be required to test this hypothesis. Additionally, the spatial contiguity of the city study area vs. the MSA study area may have an influence on the selection of the random samples (Debbage & Shepherd, 2015), and this is discussed further in Chapter 8, Part 3.

Canopy Layer UHI Traverse and Land Cover Relationships

Prior to statistical analysis of the VSU-gathered CLUHI observations and following post-hoc calibration, the additional variables of dewpoint, heat index, and wet bulb globe temperature were derived from the measurements to add commonly used indicators of heat exposure (Grundstein & Cooper, 2018; Hosokawa et al., 2019; Y. Yin et al., 2020) with the thought in mind of future proposed studies evaluating these derived variables in greater depth through a lens of inter-disciplinary physical and social science.

Dewpoint (DewPt) gives the temperature at which the air will be fully saturated, and can be calculated with the following equation (Lawrence, 2005):

$$T_d = T - (\frac{100 - RH}{5})$$

where T_d = dewpoint temperature, T = dry-bulb air temperature, and RH = percent relative humidity.

Heat index (HI) temperature gives the "feels-like" temperature, and is calculated with the following equation (Rothfusz, 1990):

$$HI = -42.379 + 2.04901523T + 10.14333127R - 0.22475541TR - 6.83783x10^{-3}T^2$$
$$- 5.481717x10^{-2}R^2 + 1.22874x10^{-3}T^2R + 8.5282x10^{-4}TR^2 - 1.99x10^{-6}T^2R^2$$

where T = dry bulb air temperature (°F) and R = relatively humidity (integer percentage).

The calculation for wet bulb globe temperature (WBGT) used here (Grundstein & Cooper, 2018) does not use direct observations for solar radiation, wind speed, or natural wet bulb temperature, as these were unable to be observed with the low-cost sensors used in this study. Rather, this formula assumes a "moderately high radiation level in light wind conditions" (Australian Bureau of Meteorology, 2010). This formula was found to slightly overestimate WBGT compared to more-involved calculations, so the values calculated for this study represent what would be the worst-case scenario. The WBGT formula used is as follows:

$$WBGT = 0.567 \times Ta + 0.393 \times e + 3.94$$

where Ta = dry bulb air temperaure (°C) and e = water vapor pressure (hPa).

To calculate WBGT, water vapor pressure (e) was calculated by the following formula, derived from the Clausius-Clapeyron equation (Petty, 2008, Chapter 7):

$$e = 6.11 \times 10^{\frac{7.5 \times T_d}{237.3 + T_d}}$$

where T_d = dewpoint temperature (°C).

Following these calculations, identical Pearson correlation tests and OLS regression models were applied to the post-hoc calibrated VSU data gathered in the field. The only difference is that LST correlations and regressions were only possible for the midday collections at the time of Landsat image collection. This was done by taking 500 random sample points from each of the traverse collections and the land cover variables associated with each point, then running the statistics on the combined datasets as done for the SUHI analysis. Combined datasets were produced for each collection time of each trip, as well as for each collection time across all trips. Presented here are the results for each collection time across all trips, as well as visualizations of air temperature and relative humidity traverse observations from trip 3. The

spatial patterns and statistical results tell the same story as, and are representative of, the results from each individual trip.

For the morning traverses and across all trips, essentially zero correlation and very poor OLS model performance between any of the observations and any of the tested land cover variables presented for samples from all trips and from trip three in Tables 8 - 10. This is likely because there has been very little, if any, solar radiation input that would heat land surfaces at the time of observation.

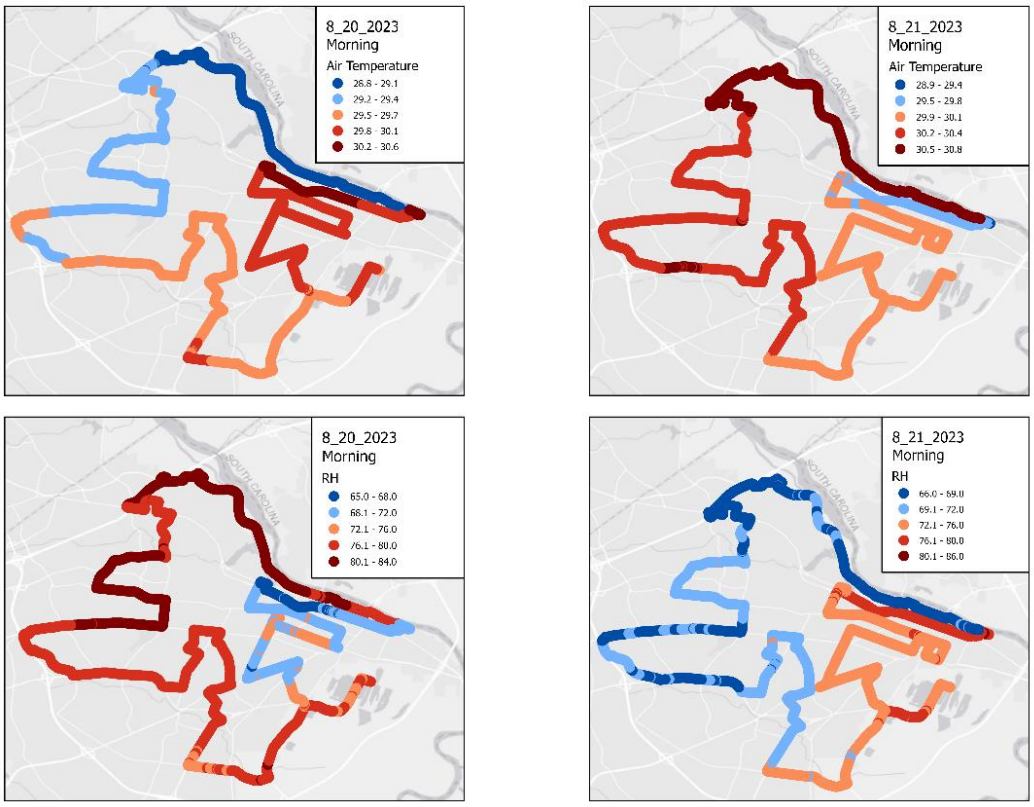

Figure 27. VSU-gathered air temperature (°C) and relative humidity (%) for the morning (7:30AM – 9:30AM) collections from trip 3 (August 20-21, 2023).

Table 8. Minimum, maximum, mean, median, and standard deviation of *all* morning observations.

All Morning Observation Collections n = 25,258					
Observation	Minimum	Maximum	Mean	Median	Standard Deviation
AirTemp	27.9	30.8	29.4	29.4	0.8
RH	65.0	97.0	78.5	78.0	7.7
DewPt	23.0	27.5	25.2	25.3	1.0
HeatIdx	33.3	37.7	35.5	35.6	0.8
WBGT	27.7	28.1	27.9	27.9	0.1
NDVI_JJA	0.1	0.4	0.2	0.2	0.1

Calculations based on all observations from each traverse collection. Trip 1 had three morning collections, Trip 2 had zero midday collections, Trip 3 had two morning collections.

NDVI values at observation points.

Table 9. Pearson correlation coefficients for 500 samples from *all* morning observations.

Pearson Correlation, All Morning Collections n = 2,500			
Parameter[1]	TreeCover	Imperv	NDVI_JJA
AirTemp_Morning	−0.048	0.046	−0.018
RH_Morning	0.088	−0.094	0.099
DewPt_Morning	0.108	−0.121	0.145
HeatIdx_Morning	0.086	−0.109	0.186
WBGT_Morning	0.112	−0.123	0.150

LST observation times correspond to midday traverse timing and thus are not included.

[1] Correlation based on 500 random samples from each traverse collection. Trip 1 had three morning collections, Trip 2 had zero morning collections, Trip 3 had two morning collections, for a total sample of 2,500 random points.

Table 10. OLS regression statistics for 500 samples from *all* morning observations.

OLS Regression Model Statistics, All Morning Collections
n = 2,500

Model[/]	R-squared	Adjusted R-squared	Resid. St.Dev	P-value
AirTemp_nlcd	0.009	0.007	0.755	< 0.05
AirTemp_tc	0.000	0.000	0.758	< 0.05
AirTemp_ndviJJA	0.002	0.002	0.757	< 0.05
AirTemp_imp	0.002	0.002	0.757	< 0.05
AirTemp_tc_imp	0.003	0.002	0.757	< 0.05
RH_nlcd	0.013	0.011	7.981	< 0.05
RH_tc	0.010	0.009	7.985	< 0.05
RH_ndviJJA	0.010	0.009	7.985	< 0.05
RH_imp	0.011	0.010	7.984	< 0.05
RH_tc_imp	0.011	0.010	7.982	< 0.05
WBGT_nlcd	0.017	0.015	0.079	< 0.05
WBGT_tc	0.023	0.022	0.078	< 0.05
WBGT_ndviJJA	0.017	0.016	0.079	< 0.05
WBGT_imp	0.023	0.022	0.078	< 0.05
WBGT_tc_imp	0.023	0.022	0.078	< 0.05

LST observation times correspond to midday traverse timing and thus are not included.

[/] Regression based on 500 random samples from each traverse collection. Trip 1 had three morning collections, Trip 2 had zero morning collections, Trip 3 had two morning collections, for a total sample of 2,500 random points.

Since the Landsat images used in the SUHI analysis were captured at approximately 11:30AM, LST observations were added to the correlations and regressions. Additionally, three bivariate OLS models for LST were tested: TC+LST, NDVI+LST, and Imp+LST. Results showed that air temperature has only very weak correlations (positive with Imp and LST, negative with TC and NDVI) with any of the land cover variables, as well as extremely poor OLS performance (Tables 11 – 14). The moisture-dependent variables (RH, DewPt, HI, and WBGT) show moderate Pearson correlation coefficients (positive for TC and NDVI, negative for Imp and LST). Again, however, OLS regressions do not perform well. At this time of the day there has been only moderate daytime heating due to solar radiation, and air temperatures are still

relatively homogeneous throughout the study area, while surface temperatures have risen more quickly.

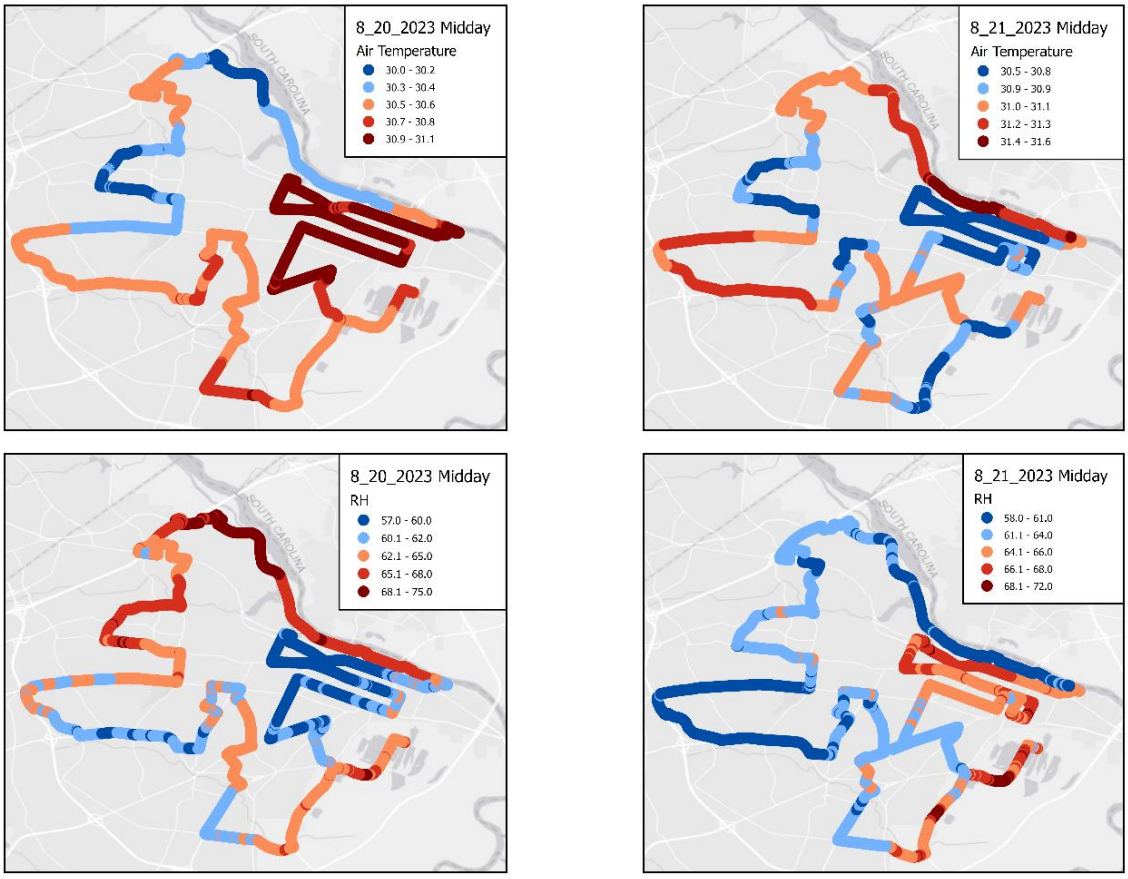

Figure 28. VSU-gathered air temperature (°C) and relative humidity (%) for the midday (11:30AM – 1:30PM) collections from trip 3 (August 20-21, 2023).

Table 11. Minimum, maximum, mean, median, and standard deviation of *all* midday observations.

All Midday Observation Collections

n = 38,242

Observation	Minimum	Maximum	Mean	Median	Standard Deviation
AirTemp	29.7	31.9	30.9	30.8	0.4
RH	40.0	80.0	63.0	63.0	3.3
DewPt	15.2	26.2	23.0	23.0	0.7
HeatIdx	30.0	38.8	35.3	35.2	0.8
WBGT	27.3	28.0	27.7	27.7	0.0
NDVI_JJA	0.1	0.4	0.2	0.2	0.1
LST_JJA	31.2	51.6	42.1	42.4	4.6

Calculations based on all obsrvations from each traverse collection. Trip 1 had three midday collections, Trip 2 had two midday collections, Trip 3 had two midday collections.

NDVI and LST values at observation points.

Table 12. Pearson correlation coefficients for 500 samples from *all* midday observations.

Pearson Correlation, All Midday Collections

n = 3,500

Parameter[1]	TreeCover	Imperv	NDVI_JJA	LST_JJA[2]
AirTemp_Midday	−0.097	0.114	−0.106	0.059
RH_Midday	0.243	−0.280	0.328	−0.297
DewPt_Midday	0.235	−0.269	0.336	−0.325
HeatIdx_Midday	0.171	−0.193	0.256	−0.256
WBGT_Midday	0.246	−0.279	0.344	−0.327

[1] Correlation based on 500 random samples from each traverse collection. Trip 1 had three midday collections, Trip 2 had two midday collections, Trip 3 had two midday collections, for a total sample of 3,500 random points.

[2] LST observation times correspond to midday traverse timing.

Table 13. OLS regression statistics for 500 samples from *all* midday observations. Land cover variables only.

OLS Regression Model Statistics, All Midday Collections

n = 3,500

Model[1]	R-squared	Adjusted R-squared	Resid. St.Dev	P-value
AirTemp_nlcd	0.014	0.013	0.382	< 0.05
AirTemp_tc	0.009	0.009	0.383	< 0.05
AirTemp_ndviJJA	0.011	0.011	0.382	< 0.05
AirTemp_imp	0.013	0.013	0.382	< 0.05
AirTemp_tc_imp	0.014	0.014	0.382	< 0.05
RH_nlcd	0.074	0.072	3.397	< 0.05
RH_tc	0.086	0.085	3.373	< 0.05
RH_ndviJJA	0.108	0.107	3.332	< 0.05
RH_imp	0.110	0.110	3.328	< 0.05
RH_tc_imp	0.110	0.110	3.328	< 0.05
WBGT_nlcd	0.078	0.076	0.048	< 0.05
WBGT_tc	0.086	0.085	0.048	< 0.05
WBGT_ndviJJA	0.118	0.118	0.047	< 0.05
WBGT_imp	0.119	0.119	0.047	< 0.05
WBGT_tc_imp	0.120	0.120	0.047	< 0.05

LST regression statistics are in separate table.

[1] Regression based on 500 random samples from each traverse collection. Trip 1 had three midday collections, Trip 2 had two midday collections, Trip 3 had two midday collections, for a total sample of 3,500 random points.

Table 14. OLS regression statistics for 500 samples from *all* midday observations. Land cover and LST variables.

OLS Regression Model Statistics, All Midday Collections

n = 3,500

Model[1]	R-squared	Adjusted R-squared	Resid. St.Dev	P-value
AirTemp_lstJJA	0.003	0.003	0.380	< 0.05
AirTemp_tc_lstJJA	0.006	0.005	0.380	< 0.05
AirTemp_lstJJA_ndviJJA	0.010	0.010	0.379	< 0.05
AirTemp_imp_lstJJA	0.007	0.006	0.380	< 0.05
RH_lstJJA	0.094	0.093	3.105	< 0.05
RH_tc_lstJJA	0.099	0.098	3.097	< 0.05
RH_lstJJA_ndviJJA	0.088	0.088	3.114	< 0.05
RH_imp_lstJJA	0.116	0.115	3.067	< 0.05
WBGT_lstJJA	0.110	0.110	0.044	< 0.05
WBGT_tc_lstJJA	0.107	0.107	0.044	< 0.05
WBGT_lstJJA_ndviJJA	0.117	0.116	0.044	< 0.05
WBGT_imp_lstJJA	0.133	0.133	0.043	< 0.05

[1] Regression based on 500 random samples from each traverse collection. Trip 1 had three midday collections, Trip 2 had two midday collections, Trip 3 had two midday collections, for a total sample of 3,500 random points.

Analysis of the afternoon observations revealed a similar story to the midday results, with a few key differences (Tables 15 - 17). By the afternoon, air temperature shows slight-to-moderate correlations with the land cover variables (positive for Imp, negative for TC and NDVI), and the correlations amongst the moisture-dependent variables all increased in magnitude from the midday. By the afternoon, air temperatures have had more time to respond to differential daytime heating across different land cover types and are less homogeneous, thereby yielding stronger correlations.

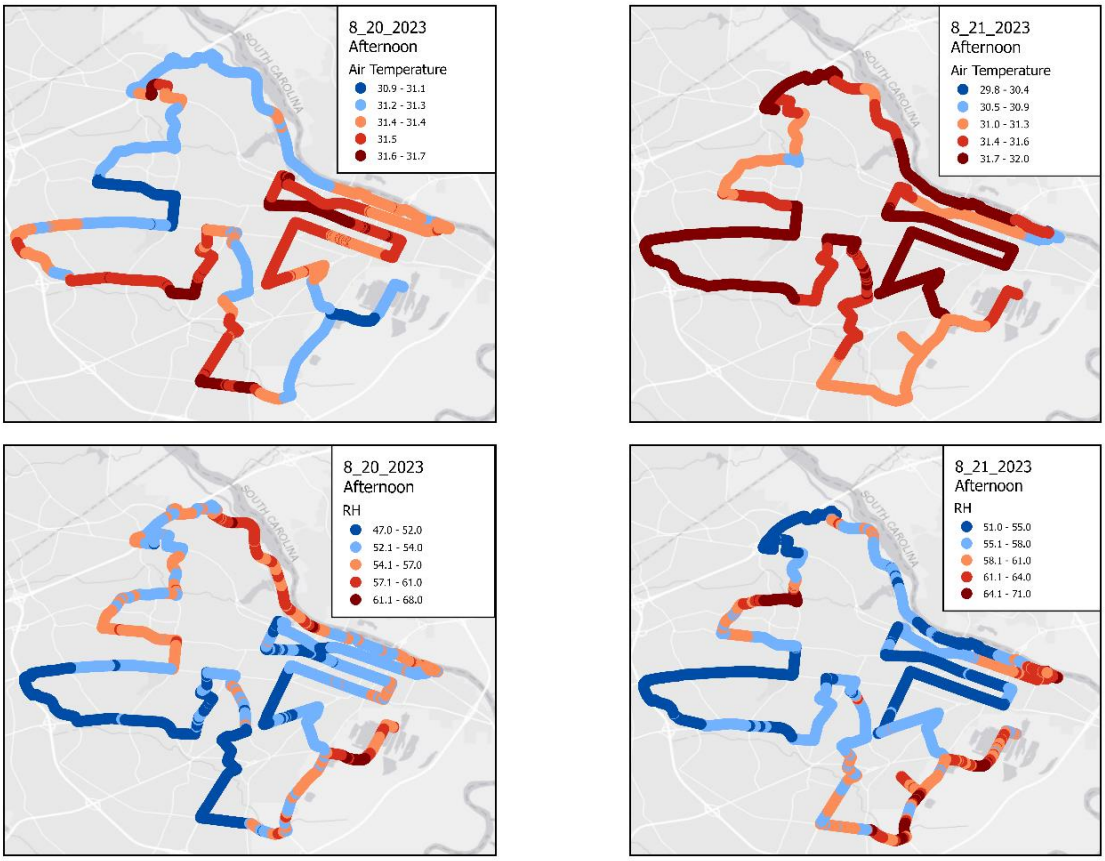

Figure 29. VSU-gathered air temperature (°C) and relative humidity (%) for the afternoon (3:30PM – 5:30PM) collections from trip 3 (August 20-21, 2023).

Table 15. Minimum, maximum, mean, median, and standard deviation of *all* afternoon observations.

All Afternoon Observation Collections

n = 30,296

Observation	Minimum	Maximum	Mean	Median	Standard Deviation
AirTemp	29.8	32.4	31.6	31.5	0.3
RH	47.0	77.0	56.3	56.0	4.2
DewPt	18.9	26.5	21.8	21.8	1.1
HeatIdx	32.8	39.8	35.1	34.9	1.0
WBGT	27.5	28.0	27.6	27.6	0.1
NDVI_JJA	0.1	0.4	0.2	0.2	0.1

Calculations based on all observations from each traverse collection. Trip 1 had one afternoon collection, Trip 2 had two afternoon collections, Trip 3 had two afternoon collections.

NDVI values at observation points.

Table 16. Pearson correlation coefficients for 500 samples from *all* afternoon observations.

Pearson Correlation, All Afternoon Collections

n = 2,500

Parameter[1]	TreeCover	Imperv	NDVI_JJA
AirTemp_Afternoon	−0.258	0.367	−0.331
RH_Afternoon	0.365	−0.418	0.459
DewPt_Afternoon	0.324	−0.354	0.408
HeatIdx_Afternoon	0.229	−0.202	0.281
WBGT_Afternoon	0.329	−0.354	0.412

LST observation times correspond to midday traverse timing and thus are not included.

[1] Correlation based on 500 random samples from each traverse collection. Trip 1 had one afternoon collection, Trip 2 had two afternoon collections, Trip 3 had two afternoon collections, for a total sample of 2,500 random points.

Table 17. OLS regression statistics for 500 samples from *all* afternoon observations.

OLS Regression Model Statistics, All Afternoon Collections

n = 2,500

Model[1]	R-squared	Adjusted R-squared	Resid. St.Dev	P-value
AirTemp_nlcd	0.127	0.125	0.321	< 0.05
AirTemp_tc	0.110	0.109	0.324	< 0.05
AirTemp_ndviJJA	0.066	0.066	0.332	< 0.05
AirTemp_imp	0.134	0.134	0.320	< 0.05
AirTemp_tc_imp	0.136	0.136	0.319	< 0.05

LST observation times correspond to midday traverse timing and thus are not included.

[1] Regression based on 500 random samples from each traverse collection. Trip 1 had one afternoon collection, Trip 2 had two afternoon collections, Trip 3 had two afternoon collections, for a total sample of 2,500 random points.

By the night data collections, weak correlations were retained for temperature and relative humidity, with air temperature having the strongest of the weak correlations at this time. These observed correlations may likely be due to the nighttime effects of the SUHI, where natural land cover tends to cool more quickly than impervious surfaces. However, OLS regression models again show extremely weak performance (Tables 18 - 20).

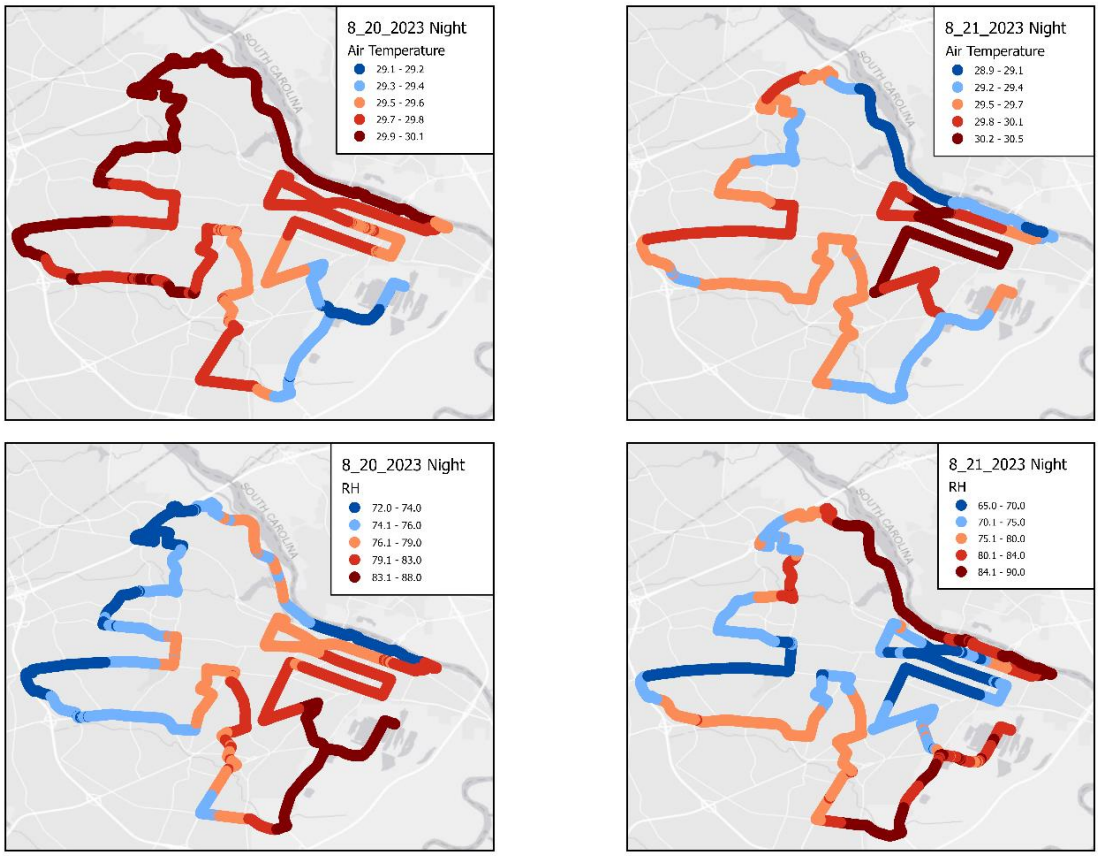

Figure 30. VSU-gathered air temperature (°C) and relative humidity (%) for the nighttime (9:00PM – 11:00PM) collections from trip 3 (August 20-21, 2023).

Table 18. Minimum, maximum, mean, median, and standard deviation of *all* night observations.

All Night Observation Collections

n = 27,930

Observation	Minimum	Maximum	Mean	Median	Standard Deviation
AirTemp	28.8	30.7	29.8	29.8	0.4
RH	65.0	94.0	78.3	78.0	5.1
DewPt	23.1	28.0	25.6	25.7	0.9
HeatIdx	34.1	39.2	36.5	36.5	0.9
WBGT	27.7	28.1	27.9	27.9	0.1
NDVI_JJA	0.1	0.4	0.2	0.2	0.1

Calculations based on all observations from each traverse collection. Trip 1 had one night collection, Trip 2 had two night collections, Trip 3 had two night collections.

NDVI values at observation points.

Table 19. Pearson correlation coefficients for 500 samples from *all* night observations.

Pearson Correlation, All Night Collections

n = 2,500

Parameter[1]	TreeCover	Imperv	NDVI_JJA
AirTemp_Night	−0.153	0.217	−0.240
RH_Night	0.105	−0.188	0.264
DewPt_Night	0.067	−0.141	0.225
HeatIdx_Night	−0.021	−0.019	0.100
WBGT_Night	0.070	−0.145	0.229

LST observation times correspond to midday traverse timing and thus are not included.

[1] Correlation based on 500 random samples from each traverse collection. Trip 1 had one night collection, Trip 2 had two night collections, Trip 3 had two night collections, for a total sample of 2,500 random points.

Table 20. OLS regression statistics for 500 samples from *all* night observations.

OLS Regression Model Statistics, All Night Collections

n = 2,500

Model[1]	R-squared	Adjusted R-squared	Resid. St.Dev	P-value
AirTemp_nlcd	0.046	0.044	0.363	< 0.05
AirTemp_tc	0.058	0.057	0.360	< 0.05
AirTemp_ndviJJA	0.023	0.023	0.367	< 0.05
AirTemp_imp	0.047	0.047	0.362	< 0.05
AirTemp_tc_imp	0.048	0.047	0.362	< 0.05
RH_nlcd	0.038	0.035	4.950	< 0.05
RH_tc	0.070	0.069	4.861	< 0.05
RH_ndviJJA	0.035	0.035	4.951	< 0.05
RH_imp	0.070	0.070	4.861	< 0.05
RH_tc_imp	0.074	0.073	4.851	< 0.05
WBGT_nlcd	0.024	0.022	0.065	< 0.05
WBGT_tc	0.053	0.052	0.064	< 0.05
WBGT_ndviJJA	0.021	0.021	0.065	< 0.05
WBGT_imp	0.055	0.054	0.064	< 0.05
WBGT_tc_imp	0.060	0.059	0.064	< 0.05

LST observation times correspond to midday traverse timing and thus are not included.

[1] Regression based on 500 random samples from each traverse collection. Trip 1 had one night collection, Trip 2 had two night collections, Trip 3 had two night collections, for a total sample of 2,500 random points.

Across all of the observation dates and times, NDVI, taken as a proxy for overall vegetation cover shows the strongest correlations to all observed variables, with one exception being that air temperature is more correlated with impervious surface coverage at night. It should be noted that these results may be influenced by the fact that all of the CLUHI traverse data was gathered from the roads, and not directly on top of any natural land cover. Therefore, this analysis may have been limited by the footprint of the observations, as it would be unrealistic to assume that the air temperature and relative humidity are not affected by radiant heat from the roadways and waste heat from other vehicles. However, these results do still suggest that there are relationships between land cover and near-surface air temperature and relative humidity.

UAS-Based Canopy Layer UHI Observations

As this study into exploiting UAS-based low-cost sensors was primarily intended as an exploratory study into the usefulness and practicality of deploying UAS in an urban environment, only qualitative visual analyses were conducted on the UAS data presented in Figures 27 - 34.

Prior to plotting the observations, post-hoc calibration was applied to the raw data. Additionally, pressure-altitude was calculated via the barometer equation (Petty, 2008, Chapter 4) which assumes the US Standard Atmosphere constant lapse rate of 0.0065 K/m. The formula is given as follows:

$$h = \frac{T_0}{\Gamma}(1 - (\frac{p}{p_0})^{0.19026})$$

where h = height AGL (meters), T_0 = air temperature at the surface (Kelvin), p = pressure at altitude to be calculated (mb), and p_0 = reference pressure at the surface (mb).

Comparing the RH profiles from the different flight locations, it appears that locations with greener, healthy vegetation ground cover and less impervious surfaces develop a low-level (< 20 meters AGL) moisture inversion (flight points 1 and 2). Flight points 7 and 8 are also over relatively healthy-appearing vegetation, though more impervious surface cover at those points seem to temper or eliminate the low-level moisture inversion. Flight points 3, 4, 5, and 6 are above barren vegetation and more impervious surface cover and do not appear to display low-level moisture inversions. These trends suggest that evapotranspiration from vegetation has a strong influence on near-surface moisture conditions.

Close inspection of the temperature profiles suggests that land cover type also has a slight, but noticeable effect on near-surface (< 15 meters AGL) temperature profiles. It appears that flight points 1, 2, 7, and 8 have a more stable near-surface lapse rate over healthy vegetation

than flight points 3, 4, 5, and 6 show over less healthy vegetation and more impervious surface cover. At flight points 3, 4, 5, and 6, near-surface temperatures dropped fairly quickly just above the surface before leveling out to a more stable lapse rate, closer to what is seen at the other flight points. This trend suggests that impervious surfaces have the effect of artificially elevating near-surface air temperatures before equilibrating to a more stable lapse rate. Flight point 2 had the healthiest-looking surrounding vegetation and showed near-zero temperature lapse rates for the first 10-20 meters on both flights. This, along with the observed low-level moisture inversion suggests that higher moisture content in the air, likely due to plant evapotranspiration, could serve as an insulator that stabilizes air temperature.

As flight point 7 was able to be flown three times during collection (12:39 PM, 5:44 PM, and 7:28 PM), this was able to provide evidence of a diurnal cycle of heating and cooling and varying moisture profiles. Flight point 7 was over a mix of green grass and a large parking lot, and the observed temperature profiles for the first and second flights relatively stable lapse rates, while the third flight in the evening showed a near-zero temperature lapse rate. Flight point 7 also showed unique moisture profiles. The morning moisture profile shows a very minor, very low-level moisture inversion, the moisture lapse rate is fairly stable. The afternoon moisture profile shows very little change in relative humidity until approximately 100 meters AGL, before increasing slightly near the peak altitude of the flight. The evening moisture profile is especially interesting, showing a profile that is opposite of the two earlier flights. In the evening flight, relative humidity showed a noticeable increase below 10 meters AGL, and then showed a negative lapse rate before mostly stabilizing by approximately 80 meters AGL. It is possible that spatial contiguity of lots of healthy grass right beside a large parking lot at flight point 7 may influence temperature and moisture fluxes over the two surfaces if there is a breeze blowing from

the grass to the pavement or vice-versa, though more thorough quantitative analysis would be required to confidently draw such conclusions.

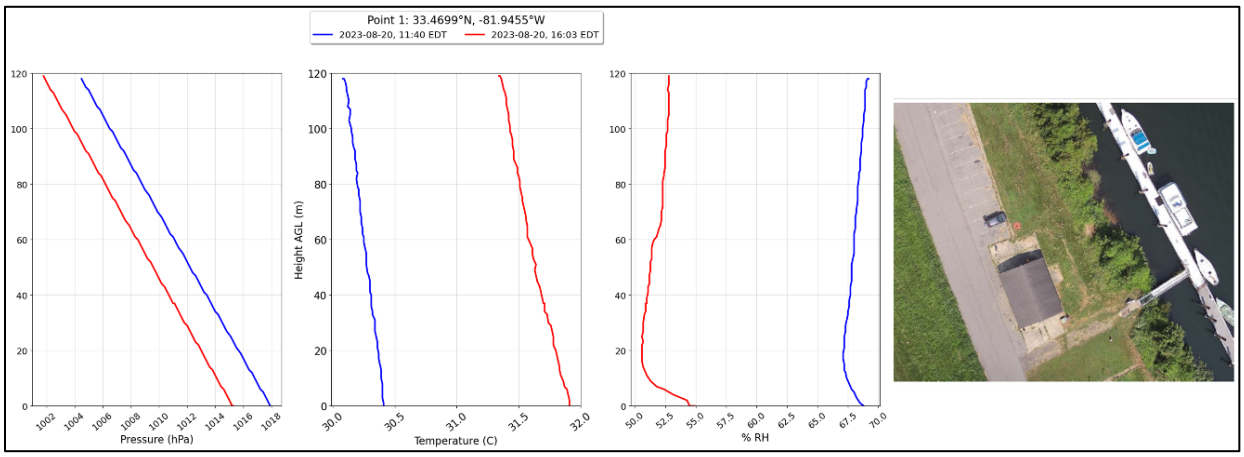

Figure 31. UAS flight point 1 data and aerial image.

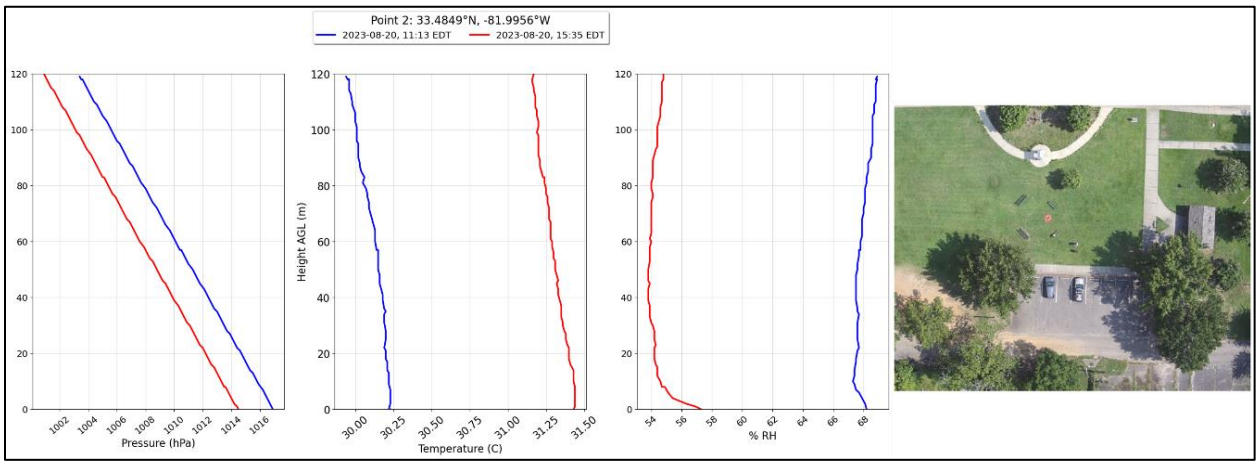

Figure 32. UAS flight point 2 data and aerial image.

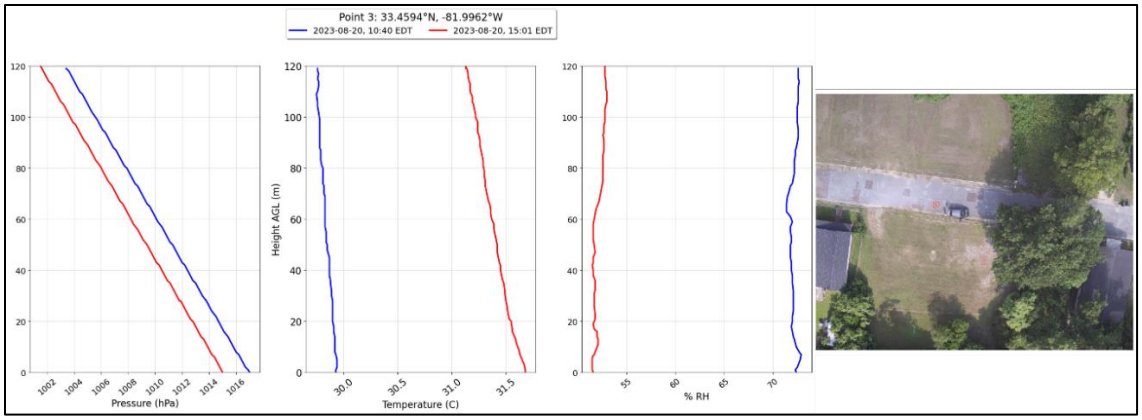

Figure 33. UAS flight point 3 data and aerial image.

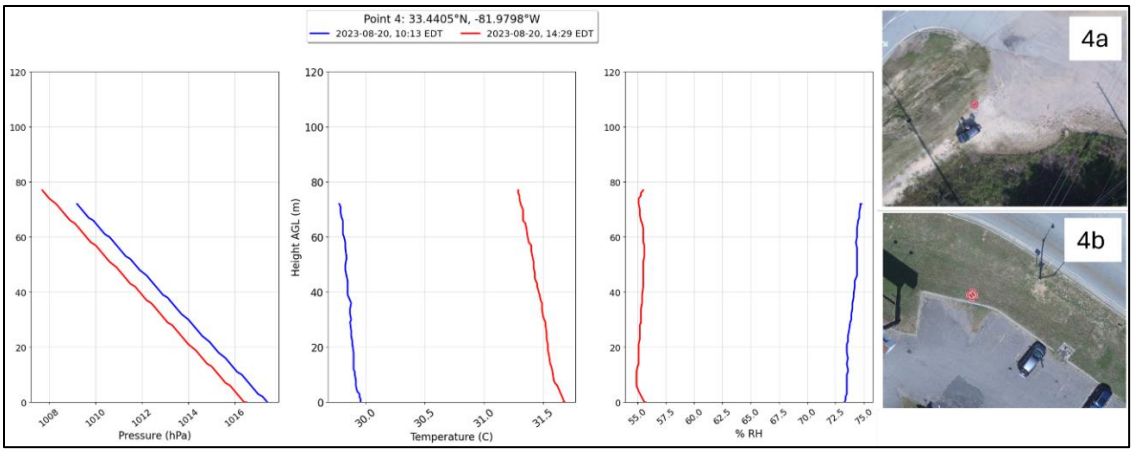

Figure 34. UAS flight points 4a and 4b and aerial images.

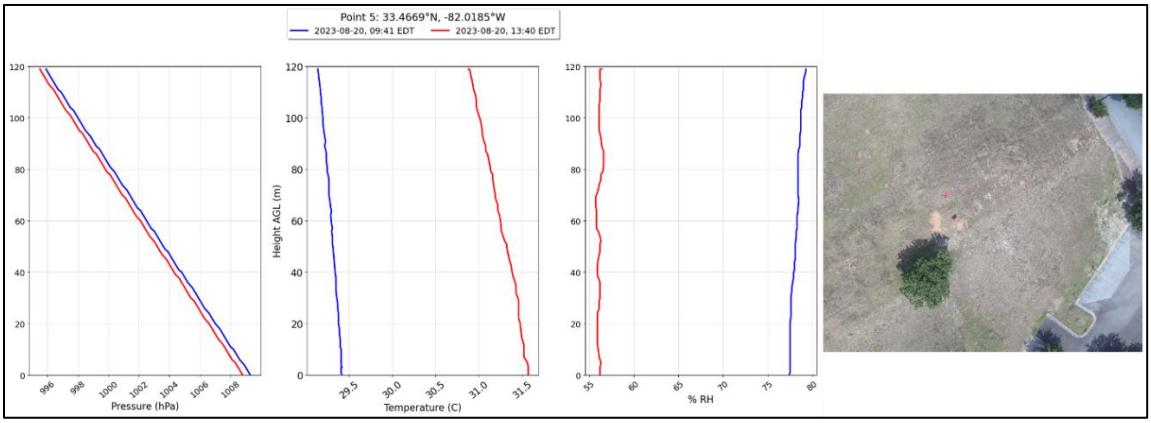

Figure 35. UAS flight point 5 data and aerial image.

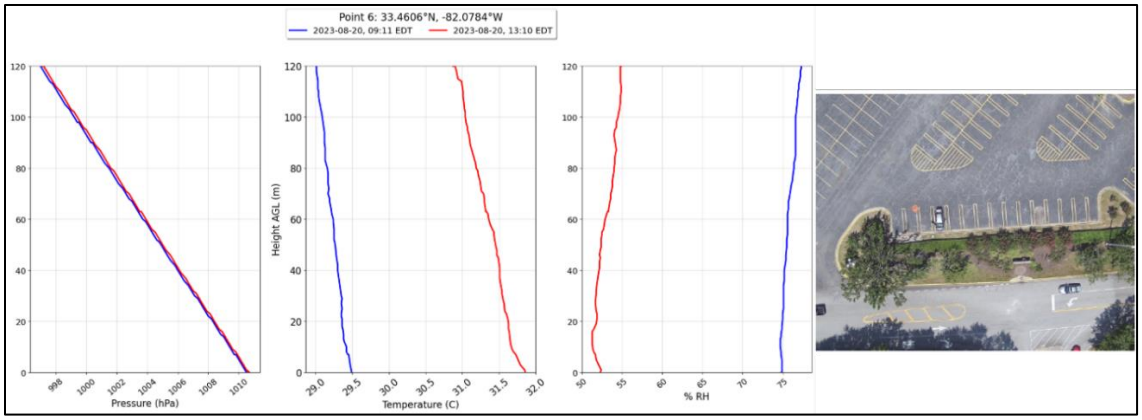

Figure 36. UAS flight point 6 data and aerial image.

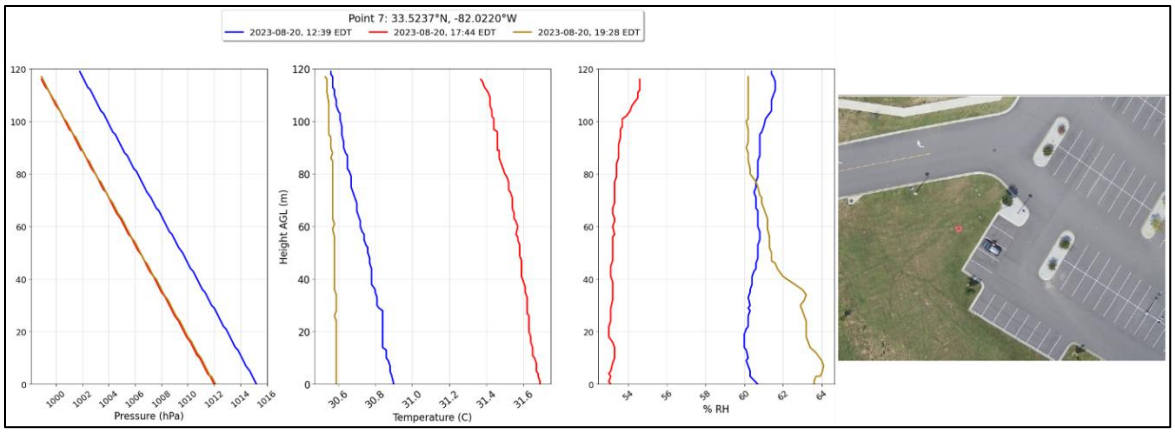

Figure 37. UAS flight point 7 data and aerial image.

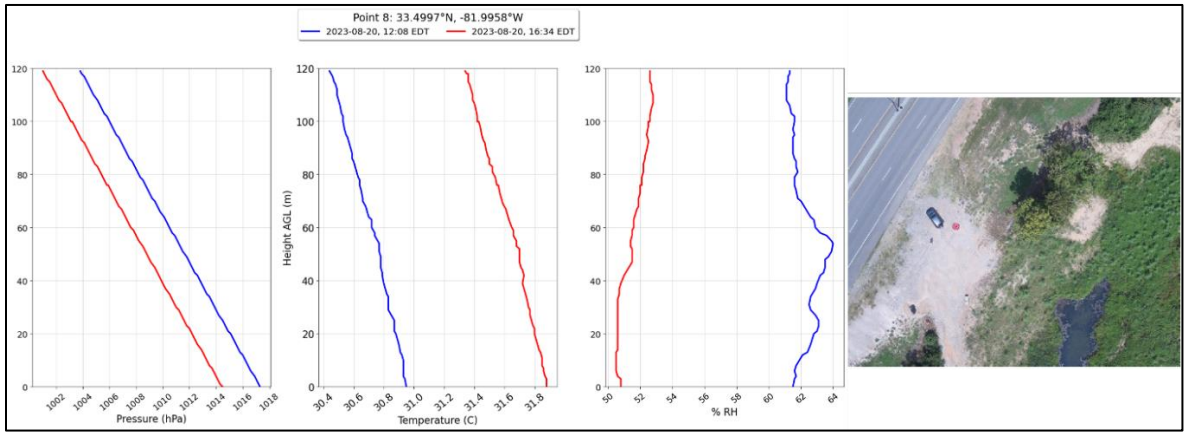

Figure 38. UAS flight point 8 data and aerial image.

CHAPTER 8

DISCUSSION

Part 1: Exploiting SUHI observations to inform CLUHI observation plans

Recent observations of the SUHI intensity and spatial patterns within Augusta showed a peak SUHI intensity of 15.1ºC from 2019 – 2021 for the whole metropolitan statistical area, as well as a clear hot spot in the central urban core of the city. Observations of the intra-SUHI intensity in the central urban core for the summer of 2020 showed a highly complex anatomy of hot and cold spots that visually appear to display the hottest surface temperatures in industrial areas and places with high impervious surface cover, and cold place appear to be collocated with greenspace and water. Of slight note, the famed Augusta National golf course does not exhibit a cool signature in these observations, even though it is almost entirely manicured green grass and decorative shrubbery. Turfgrass evapotranspiration (ET) rates are affected by mowing height, with taller grasses showing higher ET rates than short grasses (*review by* Huang & Fry, 2000), and recent observations suggest that lower ET rates are correlated with higher LST in urban environments (Danda et al., 2023). This suggests that natural land covers that are intensely maintained, with grass kept short, may not provide a cooling effect on SUHI intensity that is typically associated with natural land covers (Šalkovič & Pauditšová, 2023; Yuan & Bauer, 2007; Zhou et al., 2014).

By integrating these observations with visible imagery, a well-informed data collection campaign was able to be planned for the summer of 2023 to collect CLUHI observations in the central urban core in Augusta. With thought in mind that future studies stemming from this

project will investigate the UHI in Augusta through a socioeconomic and social equity lens, a 49.7-mile traverse was delineated that would cover areas that showed an intra-SUHI signature. Additionally, these observations aided to inform UAS flight point planning by also highlighting hot and cold intra-SUHI areas of interest along the planned traverse for flights.

Part 2: Urban heat relationships to land cover in Augusta

Statistical analysis of two sets of 500 random sample points, via Pearson correlation coefficients and OLS regression models, from the SUHI in the Augusta MSA and the central urban core indicate the existence of complex relationships between LST and land cover variables (percent tree cover, percent impervious surface, NDVI), echoing findings by previous studies (Buyantuyev & Wu, 2010; Han et al., 2021; Yuan & Bauer, 2007; Zhou & Shepherd, 2010; Zhou et al., 2014). These findings showed that tree cover percent and NDVI had moderate-to-strong negative relations with LST, and impervious surface percent showed moderate-to-strong positive relationships with LST. Evidence for the potential influence of spatial contiguity is noticed in the results (Debbage & Shepherd, 2015) Both the central urban core sample points and the MSA sample points showed approximately the same relations between LST and percent tree cover, which is likely due to the fact that, although there is overall less tree cover in the city, the urban core does have a lot of trees, meaning that both random sample datasets have similar opportunities to sample trees. However, the results show that impervious surface cover in the urban core is more influential than for the whole MSA, also that NDVI is less influential in the urban core than for the whole MSA. This is likely because there is a much higher concentration of impervious surface coverage and overall less vegetation (all vegetation, trees included) in the urban core than in the whole MSA. One specific observation should be noted. Between the summer of 2020 and the summer of 2023, peak SUHI intensity and intra-SUHI thresholds

greatly increased. These changes appear to have been driven primarily by one very large industrial manufacturing facility, and other industrial areas also showed less intense increases. The most likely explanation for this trend is that operations at these facilities were greatly decreased or halted during the summer of 2020 when lockdowns were ordered due to the COVID-19 pandemic, similar to findings in China following the lockdowns (Liu et al., 2022).

Identical statistical analyses applied to in-situ CLUHI observations, gathered across three field trips during the summer of 2023, showed less-clear relationships between observations (air temperature, relative humidity, dewpoint, heat index, and wet bulb globe temperature) and land cover (percent tree cover, percent impervious surface, NDVI, and NLCD category). Due to the fact that Landsat 8 and Landsat 9 acquire images of Augusta around 11:30 AM, analysis against LST was only possible for the midday (11:30 AM – 1:30 PM) data collections. Analysis of observations gathered in the morning (7:30 AM – 9:30 AM) from each trip and sampled across the summer showed essentially zero relationship with land cover, likely because this is typically the coolest time of day for both air and surface temperatures, due to low solar angle and minimal absorption of solar radiation by the land surfaces, and conditions as a whole are relatively homogeneous. The midday observations indicate only a weak relationship between air temperature and the tested land cover variables, and essentially zero correlation with LST. This may indicate a lag between the response times of LST and air temperature to solar input, with LST warming quicker in response to increasing solar angle than air temperature. Moisture-dependent observations (relative humidity, dewpoint, heat index, and wet bulb globe temperature) showed slight positive relations to tree cover and NDVI, and slight negative relations to impervious surface cover and LST. By this time of the day there has been moderate daytime surface heating, and differential heating of the land surface is occurring. However, air

temperatures are still relatively homogeneous across the area and have likely not yet had enough time to respond to surface heating. Afternoon observations (3:30 PM – 5:30 PM) share a similar story to the midday for moisture-dependent variables, but with slightly stronger relations to land cover variables as moisture conditions become more heterogeneous, possibly due to moisture near the surface increases from plant evapotranspiration during the daytime hours. By the afternoon, air temperature shows slight-to-moderate negative relations with tree cover and NDVI (likely due to shade and/or evaporative cooling effects), and slight-to-moderate relations with impervious surface cover. Although LST observations from Landsat are not available for this observation time, these slight-to-moderate relations with air temperature suggest that afternoon air temperatures would be more closely related to LST in the afternoon than in the midday. Night observations revealed only slight correlations between all observed variables with land cover. By this time, relations with moisture-dependent variables were weaker than for air temperature, though the relations for air temperature are still slight. The fact that air temperature maintains at least some relationship to the tested land covers provides evidence for some relationship between the nighttime CLUHI and nighttime SUHI, although this was unable to be directly observed with the choice of satellite imagery.

A few caveats must be mentioned regarding the results from the CLUHI observations. The biggest limitation to these results is that the footprint of the in-situ observations was almost entirely on paved roads, which could foreseeably impart a warm bias on the results, but this hypothesis cannot be confidently tested without data collected away from roads. Y. Yin et al. (2021) worked around this by equipping volunteers with backpack-clipped temperature sensors, but this method would be impractical for just one researcher to carry out. Additionally, the fact that a traverse was chosen over a rural-urban-rural transect means that urban-rural comparisons

are difficult to make. However, since the gathered data will likely be utilized in future studies relating to differentials in heat exposure between neighborhoods, these drawbacks were deemed to be acceptable for the purposes of this study.

Part 3: Low-cost sensors for UHI investigation

Working with an equipment budget of $500, this study deployed Raspberry Pi-based low-cost temperature, pressure, and relative humidity sensors. Unique challenges were faced in the development and deployment of these systems. For one, the author was almost entirely unfamiliar with the design and programming of Raspberry Pi systems at the beginning of this study. To aid beginners that are just beginning to learn about Raspberry Pi development, the supplier of the components (https://www.adafruit.com/) has a wealth of online resources and code examples for nearly every piece of hardware that they sell, and this was sufficient to become comfortable with the design and programming to get the system going. The biggest challenge presented by the low-cost sensors was ensuring that the data is accurate and trustworthy for analysis. Previous studies have reported that the chosen sensors are accurate and reliable for scientific data collection on a UAS (Chang et al., 2020; Chodorek et al., 2021), but calibration tests on the sensors and microcontroller used in this study revealed poor sensor performance (possibly due to daisy-chain construction) that required correction factors to be obtained via OLS regressions and fitted to observations post-hoc. Following the tests, regression model fits yielded acceptable accuracy of ± 0.25ºC for air temperature and ± 1.56% for relative humidity. Pressure readings required no correction. It is possible that the differences between sensors observed by this study and others could be due in part to the construction of the system used here. The sensors used here were daisy-chained together by plug-and-play cables compatible with the microcontroller used, and it is possible that connecting the sensors by this

method introduces signal interference into the system that would affect the accuracy of the readings. However, an in-depth electronics investigation into this was not a part of this study, and correction factors calculated against a trusted weather station were sufficient to bring accuracy to a comparable level.

Low-cost sensors can present researchers with unique advantages over traditional observation equipment. The primary areas where low-cost sensors excel are their price and their versatility for deployment. For the price of one off-the-shelf sensor system, often several low-cost systems that record the same observations. This is particularly valuable to both low-budget deployments and large-scale, multi-sensor deployments over a wide area. Additionally, low-cost sensor systems are fully custom, and allow researchers full control over how the system is housed and deployed, which is a major advantage for many novel deployment methods. This was particularly the case for this study where unique sensor housings were required to affix the sensors to the collection vehicle and the UAS.

While low-cost sensors offer several advantages of traditional off-the-shelf systems, there are also trade-offs that need to be made. Namely, there is no manufacturer guarantee of accuracy and measurements need to be verified by the researchers prior to analysis. Additionally, there is no customer support for a low-cost system that is designed and developed by researchers for their own projects.

When weighing the costs and benefits of choosing a low-cost system compared to an off-the-shelf system, the choice between the two appears to be highly project dependent. For projects that are working with a low budget or working towards a large-scale field deployment where lots of identical units are needed, low-cost sensors seem to be the better choice. Low-budget projects benefit the most from low-cost systems, as it may simply not be possible to purchase off-the-

shelf equipment which leaves observation opportunities to be wasted. If it weren't for low-cost sensors, the field campaign conducted in this study would not have been possible. However, for projects with a higher budget would do better to choose off-the-shelf systems, as their ease of use and manufacturer-guaranteed accuracy eliminates the time-intensive design, prototyping, and verification that comes with using low-cost systems.

Part 4: UAS for UHI investigation

As the current literature base for exploiting UAS for meteorological observations is very limited (Samad et al., 2022; Varentsov et al., 2023), and searches did not reveal any literature for studies intending to observe multiple flight points in an urban environment throughout the day, the methods developed and tested here are nearly entirely novel. Fortunately, best-use practices have been proposed and tested for appropriate placement of sensors and housing design on a UAS with low-cost sensors (Chang et al., 2020; Chodorek et al., 2021; Fiebrich et al., 2021). When it is not possible to elevate the temperature, pressure, and relative humidity sensors above the UAS body, the next-best option is to place it underneath the UAS body, but isolated from radiant heat off of the UAS body. As this study required the UAS to be unpacked and repacked at each flight point, mounting the sensors below the UAS body was determined to be the best option.

As this data collection was primarily intended as an exploration into the feasibility of UAS deployment by these methods in an urban environment, a few key lessons were learned. Attempting to fly multiple locations at least twice during the course of day with just one UAS and pilot available to this study presented unique challenges, namely to data continuity. Similar studies could greatly benefit from having at least two UAS and two pilots to aid in temporal continuity between flight points. Another lesson learned was that flying a UAS in an urban area

attracts attention from residents and passers-by, some good and some not-so-good. The majority of the attention drawn was curiosity into what exactly was being done and was generally pleasant, if not a bit distracting to the pilot. However, one instance of bad attention was encountered on the first flight conducted at point 4 where there was a misunderstanding of public or private land, even though the piece of land in question was indicated by city maps to be public. To avoid any potential conflict, the decision was made to relocate point 4 across the street for the second flight.

This study has shown that operating a UAS for CLUHI observations shows high potential to provide valuable insights into CLUHI vertical structure and diurnal evolution. Further refinement with two or more UAS and pilots flying multiple locations at the same time would be able to produce more data that would enable detailed quantitative analyses to be conducted. Qualitatively, the results of this study suggest the existence of relationships between land cover, near-surface conditions, and canopy layer vertical structure, where healthy vegetation elevates atmospheric moisture just above the surface before rapidly decreasing up to approximately 20 meters AGL. Temperature profiles suggest that impervious surfaces have a heating effect on near surface conditions, generally keeping air temperatures relatively stable for the first 10 – 20 meters of flight before settling into a more stable lapse rate. As an exploratory analysis, this study has demonstrated the added value of integrating UAS flights into CLUHI observation by providing insight to how local microclimates can be affected by land cover and factors of spatial contiguity. Further value could be added to UAS observations in future studies by recording wind speed and direction observations to investigate potential advective effects across and between various land cover types.

CHAPTER 9

CONCLUSION

This study first investigated the SUHI and intra-SUHI intensity and spatial patterns for the Augusta, GA-SC MSA with atmospherically-corrected thermal infrared imagery from Landsat 8 and Landsat 9 for all months 2019 – 2021, as well as summer of 2020 in the central urban core of the city. Visual analysis of the results was then utilized as an aid for planning an in-situ CLUHI data collection campaign for the summer of 2023, with data being collected via vehicle-borne and UAS-mounted low-cost sensor systems. The data collection driving traverse and UAS flight points were planned to cover as many observed intra-SUHI areas as possible in a driving time of less than two hours.

Prior to the summer 2023 data collection, Raspberry Pi-based low-cost sensor systems were developed and tested, though calibration to a trusted weather had to be conducted post-hoc due to time constraints before the first scheduled deployment. Custom sensor housings were designed and built using mostly spare materials and hand tools. Special considerations were taken in the design of the housings to shield the sensors from wind and radiant heat. For the vehicle mount, this meant placing the sensors in the center of a PVC tube that was mounted perpendicular to the direction of travel and elevated from the vehicle's boundary flow, which allowed for sensor ventilation while minimizing the effects of wind at driving speeds. For the UAS mount, this meant placing the sensors below the UAS body and in such a way that they were well-isolated from radiant heat from the body. Additionally, a small fan was added to

provide active ventilation in-flight, as Samad et al. (2022) demonstrated that there is an area of still air directly underneath the UAS body while in flight.

Following a three-trip data collection campaign in the summer of 2023, statistical analyses via Pearson correlation coefficients and ordinary least squares linear regression models were conducted on the Landsat-derived SUHI and traverse-collected CLUHI observations to test for possible relationships to land cover variables such as tree cover percent, impervious surface percent, NDVI, and NLCD land cover category. Analysis of the SUHI in summer 2023 compared random samples of 500 points, one sample set from just the central urban core area and one sample set from the whole MSA that was covered by the single Landsat image footprint used for this analysis. The results of these tests reflected results of similar studies that showed a positive relationship between LST and impervious surface coverage and negative relationships between LST and tree cover and NDVI (Buyantuyev & Wu, 2010; Han et al., 2021; Yuan & Bauer, 2007; Zhou & Shepherd, 2010; Zhou et al., 2014). Comparing the differences in magnitude of the relationships between the MSA sample and the urban core sample reveal that factors of spatial contiguity may influence the observed relationships (Debbage & Shepherd, 2015). Identical statistical analyses applied to the traverse gathered CLUHI observations did not reveal such apparent relationships, though they do hint at a diurnal cycle with the lowest relations being found for the morning when air and surface conditions are as cool as they will be, and the highest relations were found in the afternoon when air and surface conditions are at or near their warmest.

This study has also successfully demonstrated the feasibility and value of deploying a UAS equipped with low-cost sensors to observe the vertical structure of the CLUHI. Though limitations were placed on this study due to having access to just one UAS and pilot in terms of

temporal continuity of the data, this problem can be solved by having multiple UAS and pilots that can fly multiple points at the same time. However, the data from this exploratory analysis suggest that CLUHI vertical structure, especially below 20 meters, may be strongly influenced by land cover and land surface temperature, as well as factors of spatial contiguity. As such, this study has demonstrated that UAS observations of the CLUHI vertical structure have the potential to greatly increase the current understanding of diurnal cycles of heating and cooling within urban areas, as well as the influence of land cover on vertical structure.

Additionally, the CLUHI observation campaign conducted here would not have been possible without the use of low-cost sensors. With a budget of $500, the purchase of just one comparable off-the-shelf system would have used nearly all of the funds available to this project and was therefore not an option. By developing custom low-cost sensor systems, it was possible to construct three identical systems and collect valuable in-situ observations of the CLUHI in Augusta. While low-cost sensors do come with drawbacks compared to off-the-shelf sensors, namely ease of use and calibration requirements, low-cost systems can enable small budgets to achieve observational goals that previously have only been achievable for high budget projects.

In summary, this study has successfully demonstrated the added value of referencing SUHI and spatial patterns during the planning stages of an in-situ CLUHI observation campaign. Additionally, this study found that NDVI has the strongest relations to LST and SUHI intensity of the tested variables in Augusta. Weak-to-moderate relationships were found between CLUHI observations and land cover variables, including an apparent diurnal cycle of influence on near-surface conditions. Finally, this study has demonstrated that the deployment of UAS in an urban environment to observe CLUHI vertical structure has strong potential to advance the science, though some refinements to methods are still required.

By taking a holistic approach to UHI observation and integrating satellite remote sensing, surface vehicle-based observations, and UAS-based observations, valuable insights are revealed into the UHI in Augusta from, quite literally, the ground-up. With the results of this study into physical drivers and effects of the UHI in Augusta, along with results from planned studies into underlying socioeconomic factors that may have neighborhood-level heat exposure impacts, it is hoped that targeted and well-informed heat mitigation strategies can be implemented that are both effective and affordable. For Augusta, these strategies would include the expansion of greenspace and the planting of trees in both residential and industrial areas. To achieve the greatest benefits, the types of vegetation to be planted in new greenspaces should be varied and made up of species that will require minimal maintenance and stay green and healthy through the summer. Once these results are combined with the planned socioeconomic investigation into the UHI in Augusta, specific vulnerable neighborhoods that will benefit the most from heat mitigation efforts can be identified and the recommendations given here can be implemented to reduce the effects of the UHI on both the environment and human health and comfort.

REFERENCES

Avdan, U., & Jovanovska, G. (2016). Algorithm for automated mapping of land surface temperature using Landsat 8 satellite data. *Journal of Sensors*, 2016. https://doi.org/10.1155/2016/1480307

Australian Bureau of Meteorology (2010). *Thermal Comfort observations*. Commonwealth of Australia, Bureau of Meteorology. http://www.bom.gov.au/info/thermal_stress/

Baak, M., Koopman, R., Snoek, H., & Klous, S. (2020). A new correlation coefficient between categorical, ordinal and interval variables with Pearson characteristics. *Computational Statistics & Data Analysis*, *152*, 107043. https://doi.org/10.1016/j.csda.2020.107043

Bärring, L., Mattsson, J. O., & Lindqvist, S. (1985). Canyon geometry, street temperatures and urban heat island in Malmö, Sweden. *Journal of Climatology*, 5(4), 433–444. https://doi.org/10.1002/joc.3370050410

Binyan, Y., Wenjie, F., Xin ,T., & Xiru, X. (2008). Study on urban heat island of Beijing using Aster Data - a quantative remote sensing perspective. *IGARSS 2008 - 2008 IEEE International Geoscience and Remote Sensing Symposium*. https://doi.org/10.1109/igarss.2008.4779610

Burke, J. D., & Shepherd, M. (2023). The urban lightning effect revealed with Geostationary lightning mapper observations. *Geophysical Research Letters*, *50*(6). https://doi.org/10.1029/2022gl102272

Buyantuyev, A., & Wu, J. (2009). Urban heat islands and landscape heterogeneity: Linking spatiotemporal variations in surface temperatures to land-cover and socioeconomic patterns. *Landscape Ecology*, 25(1), 17–33. https://doi.org/10.1007/s10980-009-9402-4

Caissie, D. (2006). The thermal regime of rivers: A Review. *Freshwater Biology*, 51(8), 1389–1406. https://doi.org/10.1111/j.1365-2427.2006.01597.x

Cardoso, R., Dorigon, L., Teixeira, D., & Amorim, M. (2017). Assessment of urban heat islands in small- and mid-sized cities in Brazil. *Climate*, *5*(1), 14. https://doi.org/10.3390/cli5010014

Chakraborty, T., Hsu, A., Manya, D., & Sheriff, G. (2019). Disproportionately higher exposure to urban heat in lower-income neighborhoods: A multi-city perspective. *Environmental Research Letters*, 14. https://doi.org/10.1088/1748-9326/ab3b99

Chang, C.C., Chang, C.Y., Wang, J.L., Pan, X.X., Chen, Y.C., & Ho, Y.J. (2020). An optimized multicopter UAV sounding technique (MUST) for probing comprehensive atmospheric variables. *Chemosphere*, 254. https://doi.org/10.1016/j.chemosphere.2020.126867

Chilson, P. B., Bell, T. M., Brewster, K. A., Britto Hupsel de Azevedo, G., Carr, F. H., Carson, K., Doyle, W., Fiebrich, C. A., Greene, B. R., Grimsley, J. L., Kanneganti, S. T., Martin, J., Moore, A., Palmer, R. D., Pillar-Little, E. A., Salazar-Cerreno, J. L., Segales, A. R.,

Weber, M. E., Yeary, M., & Droegemeier, K. K. (2019). Moving towards a network of autonomous UAS atmospheric profiling stations for observations in the Earth's lower atmosphere: The 3D mesonet concept. *Sensors*, 19(12), 2720. https://doi.org/10.3390/s19122720

Chodorek, A., Chodorek, R. R., & Yastrebov, A. (2021). Weather Sensing in an urban environment with the use of a UAV and WebRTC-based platform: A pilot study. *Sensors*, 21(21), 7113. https://doi.org/10.3390/s21217113

Danda, T. J., Kusangaya, S., Mushore, T. D., & Mujere, N. (2023). Assessing the role of evapotranspiration in reducing surface temperatures in Harare using the SEBAL algorithm. *Urban Climate*, *49*, 101442. https://doi.org/10.1016/j.uclim.2023.101442

Debbage, N., & Shepherd, J. M. (2015). The urban heat island effect and city contiguity. *Computers, Environment and Urban Systems*, *54*, 181–194. https://doi.org/10.1016/j.compenvurbsys.2015.08.002

Del Pozo, S., Landes, T., Nerry, F., Kastendeuch, P., Najjar, G., Philipps, N., & Lagüela, S. (2020). UHI estimation based on Aster and MODIS satellite imagery: First results on Strasbourg City, France. *The International Archives of the Photogrammetry, Remote Sensing and Spatial Information Sciences*, XLIII-B3-2020, 799–805. https://doi.org/10.5194/isprs-archives-xliii-b3-2020-799-2020

Dixon, P. G., & Mote, T. L. (2003). Patterns and causes of Atlanta's Urban Heat Island–initiated precipitation. *Journal of Applied Meteorology*, 42(9), 1273–1284. https://doi.org/10.1175/1520-0450

Estoque, R. C., & Murayama, Y. (2017). Monitoring Surface Urban Heat Island Formation in a Tropical Mountain City using Landsat Data (1987–2015). *ISPRS Journal of Photogrammetry and Remote Sensing*, *133*, 18–29. https://doi.org/10.1016/j.isprsjprs.2017.09.008

Fiebrich, C. A., Ziolkowska, J. R., Chilson, P. B., & Pillar-Little, E. A. (2021). Potential socioeconomic and environmental benefits and beneficiaries of UAS atmospheric profiles from a 3D mesonet. *Weather, Climate, and Society*, *13*(2), 377–391. https://doi.org/10.1175/wcas-d-20-0118.1

Gallo, K. P., Tarpley, J. D., McNab, A. L., & Karl, T. R. (1995). Assessment of Urban Heat Islands: A satellite perspective. *Atmospheric Research*, 37, 37–43. https://doi.org/10.1016/0169-8095(94)00066-m

Greenfield, J., & Thaxton, C. (2022). Data acquisition and logging system for a drone-mounted atmospheric sensor suite. *SoutheastCon 2022*. https://doi.org/10.1109/southeastcon48659.2022.9764113

Grundstein, A., & Cooper, E. (2018). Assessment of the Australian Bureau of Meteorology Wet Bulb Globe temperature model using weather station data. *International Journal of Biometeorology*, *62*(12), 2205–2213. https://doi.org/10.1007/s00484-018-1624-1

Han, J., Zhao, X., Zhang, H., & Liu, Y. (2021). Analyzing the spatial heterogeneity of the built environment and its impact on the urban thermal environment—case study of downtown Shanghai. *Sustainability*, *13*(20), 11302. https://doi.org/10.3390/su132011302

Hedquist, B. C., & Barker, C. (2016). Detecting and Mapping the Urban Heat Island in a Small South Texas City. *The Southwestern Geographer*, *19*, 15–27.

Hosokawa, Y., Casa, D. J., Trtanj, J. M., Belval, L. N., Deuster, P. A., Giltz, S. M., Grundstein, A. J., Hawkins, M. D., Huggins, R. A., Jacklitsch, B., Jardine, J. F., Jones, H., Kazman, J. B., Reynolds, M. E., Stearns, R. L., Vanos, J. K., Williams, A. L., & Williams, W. J. (2019). Activity modification in Heat: Critical assessment of guidelines across athletic, occupational, and military settings in the USA. *International Journal of Biometeorology*, *63*(3), 405–427. https://doi.org/10.1007/s00484-019-01673-6

Hsu, A., Sheriff, G., Chakraborty, T., & Manya, D. (2021). Disproportionate exposure to urban heat island intensity across major US cities. *Nature Communications*, 12(1). https://doi.org/10.1038/s41467-021-22799-5

Huang, B., & Fry, J. D. (2000). Turfgrass Evapotranspiration. *Journal of Crop Production*, *2*(2), 317–333. https://doi.org/10.1300/j144v02n02_14

Hutcheon, R. J., Johnson, R. H., Lowry, W. P., Black, C. H., & Hadley, D. (1967). Observations of the urban heat island in a small city. *Bulletin of the American Meteorological Society*, *40*(1), 7–9.

Inoue, J., & Sato, K. (2022). Toward sustainable meteorological profiling in polar regions: Case studies using an inexpensive UAS on measuring lower boundary layers with quality of Radiosondes. *Environmental Research*, 205. https://doi.org/10.1016/j.envres.2021.112468

Jiménez-Muñoz, J. C., & Sobrino, J. A. (2010). A Single-Channel algorithm for land surface temperature retrieval from ASTER data. *IEEE Geoscience and Remote Sensing Letters, 7*(1), 176–179. https://doi.org/10.1109/LGRS.2009.2029534

Jin, M., Dickinson, R. E., & Vogelmann, A. M. (1997). A comparison of CCM2–bats skin temperature and surface-air temperature with satellite and surface observations. *Journal of Climate*, 10(7), 1505–1524. https://doi.org/10.1175/1520-0442(1997)010

Johnson, B., & Shepherd, J. M. (2018). An urban-based climatology of winter precipitation in the Northeast United States. *Urban Climate*, 24, 205–220. https://doi.org/10.1016/j.uclim.2018.03.003

Kaplan, G., Avdan, U., & Avdan, Z. Y. (2018). Urban heat island analysis using the landsat 8 satellite data: A case study in Skopje, Macedonia. *The 2nd International Electronic Conference on Remote Sensing*. https://doi.org/10.3390/ecrs-2-05171

KC, B., Shepherd, J. M., & Gaither, C. J. (2015). Climate change vulnerability assessment in Georgia. *Applied Geography*, *62*, 62–74. https://doi.org/10.1016/j.apgeog.2015.04.007

Kolath, A. S., & Egemose, S. (2023). Influences of urban discharges and urban heat effects on stream temperature. *Hydrology*, 10(2), 30. https://doi.org/10.3390/hydrology10020030

Kopec, R. J. (1970). Further observations of the urban heat island in a small city. *Bulletin of the American Meteorological Society*, *51*(7), 602–606.

Kotharkar, R. & Surawar, M. (2016). Land use, land cover, and population density impact on the formation of Canopy Urban Heat Islands through traverse survey in the Nagpur Urban

Area, India. *Journal of Urban Planning and Development*, 142(1). https://doi.org/10.1061/(asce)up.1943-5444.0000277

Landsat 4. U.S. Geological Survey. (n.d.). https://www.usgs.gov/landsat-missions/landsat-4

Landsat 8. U.S. Geological Survey. (n.d.). https://www.usgs.gov/landsat-missions/landsat-8

Landsat 9. U.S. Geological Survey. (n.d.). https://www.usgs.gov/landsat-missions/landsat-9

Lawrence, M. G. (2005). The relationship between relative humidity and the dewpoint temperature in moist air: A simple conversion and applications. *Bulletin of the American Meteorological Society*, *86*(2), 225–234. https://doi.org/10.1175/bams-86-2-225

Li, L., Zha, Y., & Wang, R. (2020). Relationship of surface urban heat island with air temperature and precipitation in global large cities. *Ecological Indicators*, *117*, 106683. https://doi.org/10.1016/j.ecolind.2020.106683

Liu, Z., Lai, J., Zhan, W., Bechtel, B., Voogt, J., Quan, J., Hu, L., Fu, P., Huang, F., Li, L., Guo, Z., & Li, J. (2022). Urban heat islands significantly reduced by Covid-19 lockdown. *Geophysical Research Letters*, *49*(2). https://doi.org/10.1029/2021gl096842

McCartney, S., Mehta, A., Shandas, V., Gallo, K., Paris, G., Nix, S., Quintero, T., Tomlinson, A., & Xian, G. (2020). *Satellite Remote Sensing for Urban Heat Islands.* NASA Applied Remote Sensing Training Program (ARSET). https://appliedsciences.nasa.gov/join-mission/training/english/arset-satellite-remote-sensing-urban-heat-islands

McLeod, J., Shepherd, M., & Appelbaum, M. (2024). Evidence of cloud and rainfall modification in a mid-sized urban area – a climatological analysis of Augusta, Georgia. *City and Environment Interactions*, *21*, 100141. https://doi.org/10.1016/j.cacint.2024.100141

Miky, Y. H. (2019). Remote Sensing Analysis for surface urban heat island detection over Jeddah, Saudi Arabia. *Applied Geomatics*, 11(3), 243–258. https://doi.org/10.1007/s12518-019-00256-9

NASA. (n.d.). *MODIS Design*. MODIS Web. https://modis.gsfc.nasa.gov/about/design.php

NASA. (n.d.). *MODIS Land Surface Temperature and Emissivity (MOD11).* MODIS Web. https://modis.gsfc.nasa.gov/data/dataprod/mod11.php

Najafzadeh, F., Mohammadzadeh, A., Ghorbanian, A., & Jamali, S. (2021). Spatial and temporal analysis of surface urban heat island and thermal comfort using landsat satellite images between 1989 and 2019: A case study in Tehran. *Remote Sensing*, *13*(21), 4469. https://doi.org/10.3390/rs13214469

Nelson, K. C., & Palmer, M. A. (2007). Stream temperature surges under urbanization and climate change: Data, models, and responses. *Journal of the American Water Resources Association*, 43(2), 440–452. https://doi.org/10.1111/j.1752-1688.2007.00034.x

Oke, T. R. (1976). The distinction between canopy and boundary-layer urban heat islands. Atmosphere, 14(4), 268–277. https://doi.org/10.1080/00046973.1976.9648422

Oke, T. R. (1982). The energetic basis of the urban heat island. *Quarterly Journal of the Royal Meteorological Society*, *108*, 1–24.

Oke, T. R. (1997). "Urban climates and global change." Applied climatology: Principles & practices, Routledge, London, 273–287.

Peng, S., Piao, S., Ciais, P., Friedlingstein, P., Ottle, C., Bréon, F.M., Nan, H., Zhou, L., & Myneni, R. B. (2011). Surface urban heat island across 419 global big cities. *Environmental Science & Technology*, *46*(2), 696–703. https://doi.org/10.1021/es2030438

Petty, G. W. (2008). Chapter 4: Atmospheric Pressure. In *A First Course in Atmospheric Thermodynamics* (1st ed., pp. 83–122). Chapter, Sundog Publishing.

Petty, G. W. (2008). Chapter 7: Moist Processes. In *A First Course in Atmospheric Thermodynamics* (1st ed., pp. 167–238). Chapter, Sundog Publishing.

Price, J. C. (1979). Assessment of the urban heat island effect through the use of satellite data. *Monthly Weather Review*, 107(11), 1554–1557. https://doi.org/10.1175/1520-0493

Qian, Y., Chakraborty, T. C., Li, J., Li, D., He, C., Sarangi, C., Chen, F., Yang, X., & Leung, L. R. (2022). Urbanization impact on regional climate and extreme weather: Current understanding, uncertainties, and future research directions. *Advances in Atmospheric Sciences*, 39(6), 819–860. https://doi.org/10.1007/s00376-021-1371-9

Qin, Z., Dall'Olmo, G., Karnieli, A., & Berliner, P. (2001). Derivation of Split window algorithm and its sensitivity analysis for retrieving land surface Temperature from NOAA-

advanced very high resolution radiometer data. *Journal of Geophysical Research Atmospheres, 106*(D19), 22655–22670. https://doi.org/10.1029/ 2000JD900452

Ramamurthy, P., & Sangobanwo, M. (2016). Inter-annual variability in urban heat island intensity over 10 major cities in the United States. *Sustainable Cities and Society*, *26*, 65–75. https://doi.org/10.1016/j.scs.2016.05.012

Ritchie, H., & Roser, M. (2018) - "Urbanization". Published online at OurWorldInData.org. Retrieved from: 'https://ourworldindata.org/urbanization' [Online Resource]

Rose, L. S., Stallins, J. A., & Bentley, M. L. (2008). Concurrent cloud-to-ground lightning and precipitation enhancement in the Atlanta, Georgia (United States), urban region. *Earth Interactions*, *12*. https://doi.org/10.1175/2008ei265.1 Rothfusz, L. P. (1990). The heat index equation (or, more than you ever wanted to know about heat index). *Fort Worth, Texas: National Oceanic and Atmospheric Administration, National Weather Service, Office of Meteorology*, 23–90. papers://c6bd9143-3623-4d4f-963f-62942ed32f11/Paper/p395

Sagris, V., & Sepp, M. (2017). Landsat-8 TIRS data for assessing urban heat island effect and its impact on human health. *IEEE Geoscience and Remote Sensing Letters*, 14(12), 2385–2389. https://doi.org/10.1109/lgrs.2017.2765703

Šalkovič, M. & Pauditšová, E. (2023). Use of Satellite Images to Determine the Temperature of Urban Surfaces for Landscape Management Purposes, Case Study Bratislava (Slovak Republic). *Land* 2023, 12, 384. https://doi.org/10.3390 land12020384

Samad, A.; Alvarez Florez,D.; Chourdakis, I.; Vogt, U. (2022). Concept of Using an Unmanned Aerial Vehicle (UAV) for 3D Investigation of Air Quality in the Atmosphere—Example of Measurements Near a Roadside. *Atmosphere*, 13, 663. https://doi.org/10.3390/atmos13050663

Santamouris, M., Ding, L., & Osmond, P. (2019). Urban Heat Island Mitigation. In P. Newton, D. Prasad, A. Sproul, & S. White (Eds.), *Decarbonising the Built Environment: Charting the Transition* (pp. 337–355). chapter, Palgrave Macmillan. https://doi.org/10.1007/978-981-13-7940-6

Shepherd, J. M. (2005). A review of current investigations of urban-induced rainfall and recommendations for the future. *Earth Interactions*, *9*(12). https://doi.org/10.1175/ei156.1

Srivanit, M., & Hokao, K. (2012). Thermal Infrared Remote Sensing for urban climate and environmental studies: An application for the City of Bangkok, Thailand. *Journal of Architectural/Planning Research and Studies (JARS)*, *9*(1), 83–100. https://doi.org/10.56261/jars.v9i1.168598

Stathopoulou, M., & Cartalis, C. (2007). Daytime urban heat islands from Landsat ETM+ and Corine land cover data: An application to major cities in Greece. *Solar Energy*, *81*(3), 358–368. https://doi.org/10.1016/j.solener.2006.06.014

Streutker, D. R. (2002). A Remote Sensing Study of the urban heat island of Houston, Texas. *International Journal of Remote Sensing*, 23(13), 2595–2608. https://doi.org/10.1080/01431160110115023

Sunardi, Fadlil, A., & Laspandi, J. D. (2019). Design and development of calculation system for normalized difference in vegetation index (NDVI) using Landsat 8 satellite image. *Journal of Physics: Conference Series*, *1373*(1), 012048. https://doi.org/10.1088/1742-6596/1373/1/012048

Tariq, A., Mumtaz, F., Zeng, X., Baloch, M. Y., & Moazzam, M. F. (2022). Spatio-temporal variation of seasonal heat islands mapping of Pakistan during 2000–2019, using day-time and night-time land surface temperatures modis and meteorological stations data. *Remote Sensing Applications: Society and Environment*, 27. https://doi.org/10.1016/j.rsase.2022.100779

U.S. Census Bureau (2020). *QuickFacts: Augusta-Richmond County consolidated government (balance), Georgia.* The Census Bureau. https://www.census.gov/quickfacts/fact/table/augustarichmondcountyconsolidatedgovernmentbalancegeorgia/POP010220

U.S. Census Bureau (2021). *American Community Survey 1-year estimates.* Retrieved from *Census Reporter Profile page for Augusta-Richmond County, GA-SC Metro Area* http://censusreporter.org/profiles/31000US12260-augusta-richmond-county-ga-sc-metro-area/

Varentsov, M., Konstantinov, P., Repina, I., Artamonov, A., Pechkin, A., Soromotin, A., Esau, I., & Baklanov, A. (2023). Observations of the urban boundary layer in a cold climate city. *Urban Climate*, 47. https://doi.org/10.1016/j.uclim.2022.101351

Wang, F., Qin, Z., Song, C., Tu, L., Karnieli, A., & Zhao, S. (2015). An improved mono-window algorithm for land surface temperature retrieval from Landsat 8 Thermal Infrared sensor data. *Remote Sensing*, 7(4), 4268–4289. https://doi.org/10.3390/rs70404268

Wong, N. H., & Yu, C. (2005). Study of green areas and urban heat island in a Tropical City. *Habitat International*, 29(3), 547–558. https://doi.org/10.1016/j.habitatint.2004.04.008

Wu, X., Wang, G., Yao, R., Wang, L., Yu, D., & Gui, X. (2019). Investigating surface urban heat islands in South America based on Modis data from 2003–2016. *Remote Sensing*, 11(10), 1212. https://doi.org/10.3390/rs11101212

Yin, Y., Grundstein, A., Mishra, D. R., Ramaswamy, L., Hashemi Tonekaboni, N., & Dowd, J. (2021). DTEX: A dynamic urban thermal exposure index based on human mobility patterns. *Environment International*, *155*, 106573. https://doi.org/10.1016/j.envint.2021.106573

Yin, Y., Tonekaboni, N. H., Grundstein, A., Mishra, D. R., Ramaswamy, L., & Dowd, J. (2020). Urban ambient air temperature estimation using hyperlocal data from Smart Vehicle-borne sensors. *Computers, Environment and Urban Systems*, 84. https://doi.org/10.1016/j.compenvurbsys.2020.101538

Yuan, F., & Bauer, M. E. (2007). Comparison of impervious surface area and normalized difference vegetation index as indicators of surface urban heat island effects in landsat imagery. *Remote Sensing of Environment*, *106*(3), 375–386. https://doi.org/10.1016/j.rse.2006.09.003

Zahn, E., Welty, C., Smith, J. A., Kemp, S. J., Baeck, M. L., & Bou-Zeid, E. (2021). The hydrological urban heat island: Determinants of acute and chronic heat stress in urban streams. *JAWRA Journal of the American Water Resources Association*, *57*(6), 941–955. https://doi.org/10.1111/1752-1688.12963

Zeiger, S., & Hubbart, J. (2015). Urban stormwater temperature surges: A central US Watershed Study. *Hydrology*, 2(4), 193–209. https://doi.org/10.3390/hydrology2040193

Zhou, B., Rybski, D., & Kropp, J. P. (2017). The role of city size and urban form in the Surface Urban Heat Island. *Scientific Reports*, 7(1). https://doi.org/10.1038/s41598-017-04242-2

Zhou, Y. & Shepherd, J. M. (2009). Atlanta's urban heat island under extreme heat conditions and potential mitigation strategies. *Natural Hazards*, 52(3), 639–668. https://doi.org/10.1007/s11069-009-9406-z

Zhou, W., Qian, Y., Li, X., Li, W., & Han, L. (2013). Relationships between land cover and the surface urban heat island: Seasonal variability and effects of spatial and thematic resolution of land cover data on predicting land surface temperatures. *Landscape Ecology*, *29*(1), 153–167. https://doi.org/10.1007/s10980-013-9950-5